

Robust feedback control of collisional plasma dynamics in presence of uncertainties

G. Albi,^{*} G. Dimarco,[†] F. Ferrarese,[‡] L. Pareschi[§]

Abstract

Magnetic fusion aims to confine high-temperature plasma within a device, enabling the fusion of deuterium and tritium nuclei to release energy. Due to the very large temperatures involved, it is essential to isolate the plasma from the device walls to prevent structural damage and the external magnetic fields play a fundamental role in achieving this confinement. In realistic settings, the physical mechanisms governing plasma behavior are highly complex, involving numerous uncertain parameters and intricate particle interactions, such as collisions, that significantly affect both confinement efficiency and overall stability. In this work, we address particularly these challenges by proposing a robust feedback control strategy designed to steer the plasma towards a desired spatial region, despite the presence of uncertainties. From a modeling perspective, we consider a collisional plasma described by a Vlasov–Poisson–BGK system, which accounts for a self-consistent electric field and a strong external magnetic field, while incorporating uncertainty in the model. A key feature of the proposed control strategy is its independence from the random parameter, making it particularly suitable for practical applications. A series of numerical simulations confirms the effectiveness of our approach and demonstrates the ability of external magnetic fields to successfully confine plasma away from the device boundaries, even in the presence of uncertain conditions.

Keywords: Vlasov-Poisson system, collisional plasma, instantaneous control, magnetic confinement, uncertainty quantification, particle methods.

Mathematics Subject Classification: 35Q83, 82D10, 65C30, 35Q93, 65M75

^{*}Department of Computer Science, University of Verona, Strada le Grazie 15, 37134 Verona, ITALY (giacomo.albi@univr.it).

[†]Department of Mathematics and Computer Science & Center for Modeling, Computing and Statistics (CMCS), University of Ferrara, via Machiavelli 30, 44121 Ferrara, ITALY (giacomo.dimarco@unife.it).

[‡]Department of Mathematics and Computer Science & Center for Modeling, Computing and Statistics (CMCS), University of Ferrara, via Machiavelli 30, 44121 Ferrara, ITALY (federica.ferrarese@unife.it).

[§]Maxwell Institute for Mathematical Sciences and Department of Mathematics, School of Mathematical and Computer Sciences (MACS), Heriot-Watt University, Edinburgh, UK (L.Pareschi@hw.ac.uk), Department of Mathematics and Computer Science & Center for Modeling, Computing and Statistics (CMCS), University of Ferrara, via Machiavelli 30, 44121 Ferrara, ITALY (lorenzo.pareschi@unife.it).

Contents

1	Introduction	2
2	Problem setting and numerical methods	5
2.1	Control of the Vlasov–Poisson–BGK model with uncertainties	6
2.2	A stochastic collocation particle-MC method	8
3	Robust feedback control by an external magnetic field	11
3.1	Derivation of an approximated feedback control	12
3.2	Realization of the control via spatial interpolation	15
4	Numerical experiments	17
4.1	2D Sod shock tube test	18
4.1.1	Accuracy of the stochastic collocation method	18
4.1.2	Effectiveness of the control strategy	19
4.2	Kelvin-Helmholtz instability	29
4.2.1	Uncontrolled case	30
4.2.2	Feedback controlled case	30
5	Conclusions	33
A	Comparison of different robust control strategies	34

1 Introduction

In recent years, considerable effort has been devoted to the development of advanced numerical methods aimed at addressing the complex challenges arising in plasma physics simulations [11, 19, 21, 33, 24]. A particular focus has been placed on the study of magnetized plasmas, due to their relevance in fusion energy applications, notably in confinement devices such as Tokamaks and Stellarators [49, 21, 50]. These devices rely on complex magnetic field configurations to confine and stabilize plasmas at very high temperatures. Reaching and maintaining optimal plasma conditions such as temperature, density, and confinement time is essential for the success of fusion experiments. However, the intrinsic complexity of plasma dynamics, characterized by turbulence, nonlinearity, and rapid transitions, combined with the influence of magnetic fields, poses important challenges both from the technical as well as from the simulation point of view [18, 20]. Addressing these issues demands the design and the use of new numerical schemes and multi-scale modeling strategies capable of accurately capturing the evolution of magnetized plasmas [4, 5, 12, 17, 10]. Additionally, the presence of uncertainty, ranging from limited knowledge of parameter settings, measurement errors in the magnetic field, the inability to define the exact initial

configuration of the plasma, or the lack of accurate models to describe interactions with boundaries, to name a few, further complicates the analysis of the system. Nevertheless, such sources of uncertainty must be accounted for in the simulations [41, 42, 26, 27, 59, 58].

In this work, to describe the time evolution of the plasma flow under uncertain conditions, we consider a Vlasov–Poisson–BGK system, which models the dynamics of charged particles subject to a self-consistent electric field, an externally applied magnetic field, and collisional effects described through a relaxation toward thermodynamic equilibrium [48, 17, 16, 14, 51, 25]. Specifically, we focus on the time evolution of negatively charged particles, i.e. electrons, while we suppose the ions to constitute a fixed background. In this case, the governing equations read:

$$\begin{aligned} \partial_t f(t, \mathbf{x}, \mathbf{v}, \mathbf{z}) + \mathbf{v} \cdot \nabla_{\mathbf{x}} f(t, \mathbf{x}, \mathbf{v}, \mathbf{z}) + (\mathbf{E}(t, \mathbf{x}, \mathbf{z}) + \\ + \mathbf{v} \times \mathbf{B}_{ext}(t, \mathbf{x})) \cdot \nabla_{\mathbf{v}} f(t, \mathbf{x}, \mathbf{v}, \mathbf{z}) = \frac{1}{\varepsilon} \mathcal{Q}(f(t, \mathbf{x}, \mathbf{v}, \mathbf{z})), \\ - \Delta_{\mathbf{x}} \phi(t, \mathbf{x}, \mathbf{z}) = \rho(t, \mathbf{x}, \mathbf{z}) - \rho_i(t, \mathbf{x}, \mathbf{z}), \quad \mathbf{E}(t, \mathbf{x}, \mathbf{z}) = -\nabla_{\mathbf{x}} \phi(t, \mathbf{x}, \mathbf{z}), \end{aligned} \quad (1.1)$$

where the ions density is space homogeneous and immutable, i.e. $\rho_i(t, \mathbf{x}, \mathbf{z}) = 1$, while the electrons density is defined by

$$\rho(t, \mathbf{x}, \mathbf{z}) = \int_{\mathbb{R}^{d_v}} f(t, \mathbf{x}, \mathbf{v}, \mathbf{z}) d\mathbf{v}, \quad (1.2)$$

with $\mathbf{z} \sim p(\mathbf{z})$ a random variable modeling the uncertainty, distributed according to a known probability density function $p(\mathbf{z})$. In this formulation, $\mathbf{E}(t, \mathbf{x}, \mathbf{z})$, is the self-consistent electric field obtained from the Poisson equation (third line of (1.1)), $\mathbf{B}_{ext}(t, \mathbf{x})$ is an external magnetic field, assumed to be independent of the uncertainty. The collision operator $\mathcal{Q}(f) = \mu(M - f)$ is of relaxation type driving the distribution f toward a local Maxwellian equilibrium $M(t, \mathbf{x}, \mathbf{v}, \mathbf{z})$ and with μ the collision frequency. The Vlasov equation (1.1) is written in non-dimensional form with ε denoting the Knudsen number, which characterizes the relative importance of collisional effects, the Debye length is chosen equal to one in the Poisson equation and thus omitted.

The above depicted dynamics, in the deterministic case, can be approximated by means of different numerical schemes ranging from finite difference, finite volume to semi Lagrangian methods [49, 15, 17, 18, 21, 47, 57, 19]. Uncertainty for the Vlasov equation has been considered for instance in [59, 37, 41]. In this paper, we focus on Particle-In-Cell (PIC) schemes [6, 22, 52, 51, 2] with the aim of designing specific control strategies in the presence of uncertainties which in turns will be handled through stochastic collocation (SC) methods [56]. In PIC simulations, the plasma is represented by a large number of particles that carry physical quantities such as electric charge and mass. These particles move through a computational grid where the electromagnetic fields are solved, [31, 32, 33, 35]. To tackle the presence of uncertainty, we introduce Gauss-Legendre nodes and use quadrature formulas [56] to compute different quantity of interests such as the expectation and the variance

with respect to the uncertain space. In addition, robust optimization techniques are used to formulate an optimal control problem that accounts for uncertainties [1]. Specifically, the goal is to design control strategies that optimize the magnetic field configuration to achieve desired plasma parameters while accounting for the variability in the system. More in details, the control problem we aim to study is given by

$$\min_{\mathbf{B}_{ext} \in \mathcal{B}^{adm}} \mathcal{J}(\mathbf{B}_{ext}; f^0; f), \quad \text{subject to} \quad (1.1), \quad (1.3)$$

where \mathcal{B}^{adm} is a set of admissible controls, f^0 the initial datum, and $\mathcal{J}(\cdot)$ is a functional which reads as follows

$$\begin{aligned} \mathcal{J}(\mathbf{B}_{ext}; f^0; f) = & \int_0^{t_f} (\mathcal{P}[\mathcal{D}(f, \psi)(t, \mathbf{z})] + \\ & + \frac{\gamma}{2} \mathcal{P} \left[\int_{\Omega} |\mathbf{B}_{ext}(t, \mathbf{x})|^2 f(t, \mathbf{x}, \mathbf{v}, \mathbf{z}) d\mathbf{x} d\mathbf{v} \right]) dt \end{aligned} \quad (1.4)$$

where

$$\mathcal{D}(f, \psi)(t, \mathbf{z}) = \int_{\Omega} \psi(\mathbf{x}, \mathbf{v}, \mathbf{z}) \left(f(t, \mathbf{x}, \mathbf{v}, \mathbf{z}) - \hat{f}(t, \mathbf{x}, \mathbf{v}) \right) d\mathbf{x} d\mathbf{v}, \quad (1.5)$$

is a running cost function, \hat{f} being a given target distribution discussed next, $\psi(\mathbf{x}, \mathbf{v}, \mathbf{z})$ a function of the state variables, $\mathcal{P}(\cdot)$ a statistical operator counting for the uncertainties, $\Omega = \Omega_x \times \Omega_v$, t_f a final prescribed time, and γ a weight penalizing the magnitude of the control given by the external magnetic field \mathbf{B}_{ext} . The scope of the functional in (1.4) is to force the distribution function or its moments towards desired values through the choice of the function $\psi(\mathbf{x}, \mathbf{v}, \mathbf{z})$. Similar problems have been investigated from an analytical perspective in recent literature, in the absence of collisions and uncertainties, see, for example, [8, 38]. From a numerical standpoint, related approaches have also been explored in [3, 30, 2, 29]. In particular, in [2] the authors of the present article, introduced a piecewise spatial control strategy based on the external magnetic field to confine a plasma governed by the Vlasov–Poisson model. The control targeted both the position and velocity of charged particles and was modeled as spatially constant but time-dependent, applied over a finite set of spatial cells. This setup reflects a physically realistic configuration, in which arbitrarily localized magnetic field values are not admissible. To design an effective instantaneous control strategy, all these constraints were explicitly incorporated into the control functional (see A for further details).

The main objective of this work is to extend the results of [2] and to develop a new optimal instantaneous control strategy in the presence of uncertainty. To the best of our knowledge, this is the first study addressing the control of out-of-equilibrium plasmas characterized by uncertain parameters. In greater detail, unlike [2], we first derive a pointwise instantaneous control that acts individually on each particle. Building on this fine-scale information, we then construct a coarse-grained control by averaging the local control

fields obtained from the minimization procedure. This yields a piecewise constant-in-space, time-dependent magnetic control field, designed to approximate the effect of the optimal microscopic control over a realistic spatial configuration and in the presence of uncertainties, as motivated in the following. We demonstrate that this approach allows for effective steering of the plasma toward desired configurations, without requiring highly complex magnetic field structures.

The remainder of the paper is organized as follows. In Section 2.1, we formulate the control problem within a two-dimensional setting, presenting its general structure and the modeling framework adopted. In Section 2.2, we introduce the numerical methods used to solve the Vlasov–Poisson system under uncertainty, with particular emphasis on Particle-In-Cell schemes and the Gauss–Legendre quadrature for handling stochastic parameters. In Section 3, we discretize the control problem and derive a strategy capable of managing both uncertainty and collisional effects. Section 4 presents a series of numerical experiments that validate the effectiveness of the proposed method. In Section 5, we summarize the main results and outline possible directions for future work. Finally, the Appendix A is devoted to the extension of the control strategy proposed in [2] to the setting with uncertainty, and to a comparison with the new approach developed in this work, highlighting the improvements and the enhanced performance achieved by the latter.

2 Problem setting and numerical methods

In a Tokamak device, plasma confinement is governed by a magnetic field that constrains the motion of charged particles. While particles move almost freely along the field lines, their perpendicular motion is restricted to rapid Larmor gyrations. The magnetic configuration is determined by two components: a dominant toroidal field, generated by coils encircling the central axis of the torus, and a weaker poloidal field, produced both by external coils and by the plasma current. Although smaller in magnitude, the poloidal field plays a crucial role in confinement, since its combination with the toroidal component yields helical magnetic field lines that prevent plasma losses [54].

To simplify the analysis, we consider a two-dimensional phase-space framework. In this context, we assume that the magnetic field lines are approximately horizontal, so that the magnetic field component under consideration is oriented orthogonally to the xy -plane. This assumption reflects the predominance of the toroidal component over the poloidal one, and allows us to capture the essential transport dynamics of the plasma while maintaining a tractable model for an axisymmetric toroidal configuration.

In this section, we first discuss the setting and then we propose a suitable numerical discretization for the Vlasov–Poisson–BGK model with uncertainties. In the following section, based on the discussed discretization, we introduce and study an instantaneous control strategy.

2.1 Control of the Vlasov–Poisson–BGK model with uncertainties

In the proposed configuration, the reference frame $(\mathbf{x}_\perp, \mathbf{v}_\perp)$ is chosen such that the external magnetic field remains always orthogonal to the plane in which the time evolution of the single-species plasma distribution function takes place, automatically ensuring that the divergence-free condition is satisfied. This gives

$$f = f(t, \mathbf{x}_\perp, \mathbf{v}_\perp, \mathbf{z}), \quad f : \mathbb{R}_+ \times \Omega_x \times \Omega_v \times \Omega_z, \quad (2.1)$$

where $\Omega_z \subseteq \mathbb{R}^{d_z}$ denotes the uncertainty space, $\Omega_x \subseteq \mathbb{R}^{d_x}$, $\Omega_v \subseteq \mathbb{R}^{d_v}$ the space and velocity domain, and where we set from now on $d_x = d_v = 2$. The evolution of $f(t, \mathbf{x}_\perp, \mathbf{v}_\perp, \mathbf{z})$ is then governed by the following collisional Vlasov-type equation

$$\begin{aligned} \partial_t f + \mathbf{v}_\perp \cdot \nabla_{\mathbf{x}_\perp} f + F(t, \mathbf{x}_\perp, \mathbf{v}_\perp, \mathbf{z}) \cdot \nabla_{\mathbf{v}_\perp} f &= \frac{1}{\varepsilon} \mathcal{Q}(f), \\ f(0, \mathbf{x}_\perp, \mathbf{v}_\perp, \mathbf{z}) &= f_0(\mathbf{x}_\perp, \mathbf{v}_\perp, \mathbf{z}), \end{aligned} \quad (2.2)$$

where f_0 denotes the initial distribution function, which depends on the uncertain parameter \mathbf{z} , assumed to follow a given probability distribution $p(\mathbf{z})$. For brevity, we omitted the explicit dependence of f on $t, \mathbf{x}_\perp, \mathbf{v}_\perp$, and \mathbf{z} in previous expression (2.2). The force field acting on the particles is given by:

$$F(t, \mathbf{x}_\perp, \mathbf{v}_\perp, \mathbf{z}) = \mathbf{E}(t, \mathbf{x}_\perp, \mathbf{z}) + \mathbf{v}_\perp \times \mathbf{B}_{ext}(t, \mathbf{x}_\perp), \quad (2.3)$$

where \mathbf{B}_{ext} is the external magnetic field, assumed to be independent of the uncertainty \mathbf{z} as already stated, and \mathbf{E} is the electric field derived from the solution of the Poisson equation:

$$\mathbf{E}(t, \mathbf{x}_\perp, \mathbf{z}) = -\nabla_{\mathbf{x}_\perp} \phi(t, \mathbf{x}_\perp, \mathbf{z}), \quad -\Delta_{\mathbf{x}_\perp} \phi(t, \mathbf{x}_\perp, \mathbf{z}) = \rho(t, \mathbf{x}_\perp, \mathbf{z}) - 1, \quad (2.4)$$

with ϕ the electric potential, and the charge density defined as:

$$\rho(t, \mathbf{x}_\perp, \mathbf{z}) = \int_{\Omega_v} f(t, \mathbf{x}_\perp, \mathbf{v}_\perp, \mathbf{z}) d\mathbf{v}_\perp. \quad (2.5)$$

The right-hand side of equation (2.2), $\mathcal{Q}(f)$, describes the collisions among particles. In this work, we adopt a BGK-type operator defined as:

$$\mathcal{Q}(f) = \mu (\mathcal{M}(t, \mathbf{x}_\perp, \mathbf{v}_\perp, \mathbf{z}) - f(t, \mathbf{x}_\perp, \mathbf{v}_\perp, \mathbf{z})), \quad (2.6)$$

where μ is the collision frequency which in general may depend upon the macroscopic quantities and the uncertain parameters, i.e. $\mu = \mu(\rho, T, \mathbf{z})$, and \mathcal{M} is the local Maxwellian equilibrium distribution given by:

$$\mathcal{M}(t, \mathbf{x}_\perp, \mathbf{v}_\perp, \mathbf{z}) = \frac{\rho(t, \mathbf{x}_\perp, \mathbf{z})}{2\pi T(t, \mathbf{x}_\perp, \mathbf{z})} \exp\left(-\frac{|\mathbf{v}_\perp - \mathbf{U}(t, \mathbf{x}_\perp, \mathbf{z})|^2}{2T(t, \mathbf{x}_\perp, \mathbf{z})}\right), \quad (2.7)$$

with \mathbf{U} , and T denoting the mean velocity and temperature, respectively, computed as:

$$\begin{aligned}\mathbf{U}(t, \mathbf{x}_\perp, \mathbf{z}) &= \frac{1}{\rho(t, \mathbf{x}_\perp, \mathbf{z})} \int_{\Omega_v} \mathbf{v}_\perp f(t, \mathbf{x}_\perp, \mathbf{v}_\perp, \mathbf{z}) d\mathbf{v}_\perp, \\ T(t, \mathbf{x}_\perp, \mathbf{z}) &= \frac{1}{2\rho(t, \mathbf{x}_\perp, \mathbf{z})} \int_{\Omega_v} |\mathbf{v}_\perp - \mathbf{U}(t, \mathbf{x}_\perp, \mathbf{z})|^2 f(t, \mathbf{x}_\perp, \mathbf{v}_\perp, \mathbf{z}) d\mathbf{v}_\perp.\end{aligned}\tag{2.8}$$

The final goal is to control the dynamics described by (2.2)-(2.4) using an external magnetic field to configure charged particles into a desired setting while keeping them as far as possible from the walls. To achieve this, we start from the following continuous control problem

$$\min_{\mathbf{B}^{ext} \in \mathcal{B}_{adm}} \mathcal{J}(\mathbf{B}^{ext}; f^0, f), \quad \text{s.t. (2.2) - (2.4) are satisfied}\tag{2.9}$$

where

$$\begin{aligned}\mathcal{J}(\mathbf{B}^{ext}; f^0, f) &= \int_0^{t_f} \mathcal{P} \left[\sum_{\ell \in \{\mathbf{x}, \mathbf{v}\}} \mathcal{D}(f, \psi_\ell)(t, \mathbf{z}) \right] dt + \\ &+ \frac{\gamma}{2} \int_0^{t_f} \mathcal{P} \left[\int_{\Omega} |\mathbf{B}^{ext}(t, \mathbf{x}_\perp)|^2 f(t, \mathbf{x}_\perp, \mathbf{v}_\perp, \mathbf{z}) d\mathbf{x}_\perp d\mathbf{v}_\perp \right] dt,\end{aligned}\tag{2.10}$$

with $\Omega = \Omega_x \times \Omega_v$, and where $\mathcal{D}(\cdot)$ aims at enforcing a specific configuration of the distribution function and of its moments, that is

$$\mathcal{D}(f, \psi_\ell)(t, \mathbf{z}) = \frac{\alpha_\ell}{2} |m(f, \psi_\ell)(t, \mathbf{z}) - \hat{\psi}_\ell|^2 + \frac{\beta_\ell}{2} m_\sigma(f, \psi_\ell)(t, \mathbf{z}),\tag{2.11}$$

with $\alpha_\ell, \beta_\ell \geq 0$ weighting parameters for $\ell = \{\mathbf{x}, \mathbf{v}\}$, and

$$\begin{aligned}m(f, \psi_\ell)(t, \mathbf{z}) &= \int_{\Omega} \psi_\ell(\mathbf{x}_\perp, \mathbf{v}_\perp, \mathbf{z}) f(t, \mathbf{x}_\perp, \mathbf{v}_\perp, \mathbf{z}) d\mathbf{x}_\perp d\mathbf{v}_\perp, \\ m_\sigma(f, \psi_\ell)(t, \mathbf{z}) &= \int_{\Omega} |\psi_\ell(\mathbf{x}_\perp, \mathbf{v}_\perp, \mathbf{z}) - m(f, \psi_\ell)(t, \mathbf{z})|^2 f(t, \mathbf{x}_\perp, \mathbf{v}_\perp, \mathbf{z}) d\mathbf{x}_\perp d\mathbf{v}_\perp.\end{aligned}\tag{2.12}$$

The first equation in (2.12) aims at enforcing the moments of the distribution function to assume some given values in different regions of the physical space through concentration of the distribution function at some given target $\hat{\psi}_\ell$. The second equation tries to minimize the distance from the average value $m(f, \psi_\ell)$ both in space as well as in velocity space around these targets.

The statistical operator $\mathcal{P}[\cdot]$ is introduced to ensure the robustness of the control strategy with respect to the uncertainty parameter \mathbf{z} . One natural choice for $\mathcal{P}[\cdot]$ is the mathematical expectation in the random space, defined as:

$$\mathcal{P}[\varphi_f(\cdot, \mathbf{z})] = \int_{\Omega_z} \varphi_f(\cdot, \mathbf{z}) p(\mathbf{z}) d\mathbf{z},\tag{2.13}$$

where $\varphi_f(\cdot, \mathbf{z})$ is a measurable quantity depending on the uncertainty \mathbf{z} . An alternative measure of robustness that we consider in this work is based on the worst-case scenario idea, which corresponds to minimizing a given macroscopic quantity related to the plasma evolution over all admissible realizations of \mathbf{z} . In this case, the operator takes the form:

$$\mathcal{P}[\varphi_f(\cdot, \mathbf{z})] = \varphi_f(\cdot, \mathbf{z}_0), \quad \text{with } \mathbf{z}_0 = \arg \max_{\mathbf{z}} T_b(\cdot, \mathbf{z}), \quad (2.14)$$

being $T_b(\cdot, \mathbf{z})$ the temperature close to the boundary for a fixed value of the uncertainty.

2.2 A stochastic collocation particle-MC method

We focus now on the numerical solution of the Vlasov equation (2.2) in the presence of uncertainty. The proposed numerical approach combines Particle-In-Cell (PIC) techniques for the transport part [9, 31] with Direct Simulation Monte Carlo (DSMC) methods to handle the collisional term [45, 46, 6, 23]. To incorporate uncertainty, several strategies have been proposed in the literature about Vlasov or related kinetic type equations with random inputs, ranging from intrusive Stochastic Galerkin methods [36, 13, 55, 28] to non-intrusive techniques such as Monte Carlo sampling [26, 27, 39]. In this work we focus on an alternative non-intrusive approach: the stochastic collocation (SC) method [56, 43] which up to our knowledge it has never been used for treating uncertainties in the context of Vlasov-type equations.

For a quantity of interest $\varphi_f(t, \mathbf{x}_\perp, \mathbf{v}_\perp, \mathbf{z})$, we first define its expected value and variance in the uncertain space as:

$$\mathbb{E}[\varphi_f](t, \mathbf{x}_\perp, \mathbf{v}_\perp) = \int_{\Omega_z} \varphi_f(t, \mathbf{x}_\perp, \mathbf{v}_\perp, \mathbf{z}) p(\mathbf{z}) d\mathbf{z}, \quad (2.15)$$

$$\sigma^2[\varphi_f](t, \mathbf{x}_\perp, \mathbf{v}_\perp) = \int_{\Omega_z} (\varphi_f(t, \mathbf{x}_\perp, \mathbf{v}_\perp, \mathbf{z}) - \mathbb{E}[\varphi_f](t, \mathbf{x}_\perp, \mathbf{v}_\perp))^2 p(\mathbf{z}) d\mathbf{z}. \quad (2.16)$$

Additional observable can be defined in the same manner. Typical quantities of interest include the distribution function f itself, as well as its moments: density, mean velocity, and temperature for example. In the latter cases, the dependence on \mathbf{v}_\perp is dropped in (2.15)-(2.16). We then select N_z quadrature nodes $\{z_k\}_{k=1}^{N_z}$ (where we suppose to use only one index to describe the multidimensional space Ω_z) with corresponding weights $\{w_k\}$ for a given quadrature rule adapted to the distribution $p(\mathbf{z})$ and solve N_z independent deterministic Vlasov problems. We also suppose, to easily describe the proposed approach, that uncertainty affects only the initial data, i.e. $f_0(\mathbf{x}_\perp, \mathbf{v}_\perp, \mathbf{z})$. For each node we have then:

$$\partial_t f^k(t, \mathbf{x}_\perp, \mathbf{v}_\perp) + \mathbf{v}_\perp \cdot \nabla_{\mathbf{x}_\perp} f^k + F^k(t, \mathbf{x}_\perp, \mathbf{v}_\perp) \cdot \nabla_{\mathbf{v}_\perp} f^k = \frac{1}{\varepsilon} Q(f^k), \quad (2.17)$$

being $F^k(t, \mathbf{x}_\perp, \mathbf{v}_\perp) = (\mathbf{E}^k(t, \mathbf{x}_\perp) + \mathbf{v}_\perp \times \mathbf{B}_{ext}(t, \mathbf{x}_\perp))$, with initial data $f_0^k = f_0(\cdot, \cdot, z_k)$. The SC method to approximate expected value and variance in the uncertain space is then obtained by the following algorithm:

Algorithm 2.1 (Stochastic collocation for the Vlasov equation with random inputs).

1. Consider N_z collocation nodes z_k and weights w_k using Gauss quadrature according to $p(\mathbf{z})$.
2. For each node z_k , solve the deterministic Vlasov problem with the preferred numerical technique to get $\tilde{f}^{k,n}$.
3. Compute the expected value and variance of the quantity of interest. For example in the case of the computation of expectation and variance for the distribution function, one has

$$E_{N_z}[\tilde{f}^n] = \sum_{k=1}^{N_z} w_k \tilde{f}^{n,k}, \quad \sigma_{N_z}^2[\tilde{f}^n] = \sum_{k=1}^{N_z} w_k \left(\tilde{f}^{n,k} - E_{N_z}[\tilde{f}^n] \right)^2.$$

Other statistics with respect the random space and related to the distribution function or its moments can be computed in the same manner.

This method benefits from spectral convergence when the solution depends smoothly on the uncertain parameter \mathbf{z} , i.e., the error decays faster than any power of N_z^{-1} , depending on regularity of the solution. The typical error estimate reads, in the case in which the other discretization errors are neglected, as:

$$|\mathbb{E}[f] - E_{N_z}[\tilde{f}]| \leq Cp^{-2N_z}$$

where C and p are two constants.

In order to approximate the N_z deterministic collisional Vlasov equations (2.17), we rely on a particle method. This approach consists first in approximating the initial condition $f_0(\mathbf{x}_\perp, \mathbf{v}_\perp)$ in (2.17) by a discrete sum of Dirac masses (we omit from now on the apex k indicating the point in the random space):

$$f_N^0(\mathbf{x}_\perp, \mathbf{v}_\perp) := \sum_{m=1}^N \omega_m \delta(\mathbf{x}_\perp - \mathbf{x}_m^0) \delta(\mathbf{v}_\perp - \mathbf{v}_m^0), \quad (2.18)$$

where $(\mathbf{x}_m^0, \mathbf{v}_m^0)_{1 \leq m \leq N}$ represent the initial positions and velocities of the particles, and ω_m are the associated particle weights. Next, we introduce a spatial discretization grid composed of M_c cells \mathcal{C}_j , $j = 1, \dots, M_c$, used to compute the electric field, together with a time discretization of the interval $[0, t_f]$ with step size $h > 0$. In this setting, the approximate solution of the Vlasov equation at time level n is given by the empirical density function:

$$f_N^n(\mathbf{x}_\perp, \mathbf{v}_\perp) = \sum_{m=1}^N \omega_m \delta(\mathbf{x}_\perp - \mathbf{x}_m^n) \delta(\mathbf{v}_\perp - \mathbf{v}_m^n), \quad (2.19)$$

where the particle positions and velocities at time level n are updated through a splitting procedure between the collision and transport steps.

The collision step is defined by:

$$\begin{cases} \partial_t f_N^* = \frac{1}{\varepsilon} \mathcal{Q}(f_N^*), \\ f_N^*(0, \mathbf{x}_\perp, \mathbf{v}_\perp) = f_N^n(\mathbf{x}_\perp, \mathbf{v}_\perp), \end{cases} \quad (2.20)$$

while the transport step is given by:

$$\begin{cases} \partial_t f_N^{**} + \mathbf{v}_\perp \cdot \nabla_{\mathbf{x}_\perp} f_N^{**} + (\mathbf{E}^{**} + \mathbf{v}_\perp \times \mathbf{B}_{ext}^{**}) \cdot \nabla_{\mathbf{v}_\perp} f_N^{**} = 0, \\ f_N^{**}(0, \mathbf{x}_\perp, \mathbf{v}_\perp) = f_N^*(\mathbf{x}_\perp, \mathbf{v}_\perp), \end{cases} \quad (2.21)$$

thus yielding the solution at time t^{n+1} :

$$f_N^{n+1}(\mathbf{x}_\perp, \mathbf{v}_\perp) = \mathcal{T}_h(\mathcal{Q}_h(f_N^n)(\mathbf{x}_\perp, \mathbf{v}_\perp)).$$

The discretization of the collision step gives:

$$f_N^*(\mathbf{x}_\perp, \mathbf{v}_\perp) = e^{-\nu h} f_N^n(\mathbf{x}_\perp, \mathbf{v}_\perp) + (1 - e^{-\nu h}) \mathcal{M}_N^n(\mathbf{x}_\perp, \mathbf{v}_\perp), \quad (2.22)$$

where $\nu = \mu/\varepsilon$ and $\mathcal{M}_N^n(\cdot)$ is the local Maxwellian distribution (2.7) computed from the knowledge of the moments of f and * indicates that (2.22) furnishes the solution of the sole collisional part (2.20) which will be then used as an initial data for the solution of the Vlasov equation (2.21). It is important to observe that the collisional term modifies only the particle velocities, while preserving the first three moments of f , namely mass, momentum, and energy. This means that \mathcal{M} is constant over the relaxation step (2.21). From a probabilistic viewpoint, relation (2.22) is interpreted as follows [44, 7]: with probability $e^{-\nu h}$, the velocity \mathbf{v}_m of a particle remains unchanged, while with probability $1 - e^{-\nu h}$, it is replaced by a velocity sampled from the local Maxwellian. This can be expressed as:

$$\mathbf{v}_m^* = \chi(\eta_m < e^{-\nu h}) \mathbf{v}_m^n + (1 - \chi(\eta_m < e^{-\nu h})) \left(\mathbf{U}_m^n + \xi_m \sqrt{T_m^n} \right), \quad (2.23)$$

where $\eta_m \sim \mathcal{U}([0, 1])$ is uniformly distributed, $\xi_m \sim \mathcal{N}(0, 1)$ is a standard normal random variable, and $\chi(\cdot)$ denotes the indicator function. Here, \mathbf{U}_m^n and T_m^n are defined as:

$$\mathbf{U}_m^n = \sum_{j=1}^{M_c} \tilde{\mathbf{U}}_j^n \chi(\mathbf{x}_m^n \in \mathcal{C}_j), \quad T_m^n = \sum_{j=1}^{M_c} \tilde{T}_j^n \chi(\mathbf{x}_m^n \in \mathcal{C}_j),$$

where:

$$\begin{aligned} \tilde{\mathbf{U}}_j^n &= \frac{1}{\tilde{\rho}_j^n} \sum_{m=1}^N \omega_m \mathbf{v}_m^n \chi(\mathbf{x}_m^n \in \mathcal{C}_j), \\ \tilde{T}_j^n &= \frac{1}{2\tilde{\rho}_j^n} \sum_{m=1}^N \omega_m |\mathbf{v}_m^n - \tilde{\mathbf{U}}_j^n|^2 \chi(\mathbf{x}_m^n \in \mathcal{C}_j), \end{aligned} \quad (2.24)$$

represent the local momentum and temperature at time t^n within cell \mathcal{C}_j , and

$$\tilde{\rho}_j^n = \sum_{m=1}^N \omega_m \chi(\mathbf{x}_m^n \in \mathcal{C}_j)$$

is the local particle density.

The transport phase in phase space is finally recovered by approximating the particle trajectories according to the characteristic curves of the Vlasov equation:

$$\begin{aligned} \frac{d\mathbf{x}_m(t)}{dt} &= \mathbf{v}_m(t), \\ \frac{d\mathbf{v}_m(t)}{dt} &= \mathbf{E}(t, \mathbf{x}_m) + \mathbf{v}_m \times \mathbf{B}_{ext}(t, \mathbf{x}_m). \end{aligned} \tag{2.25}$$

Here, the electric field $\mathbf{E}(t, \mathbf{x})$ is obtained by approximating the Poisson equation with a finite difference method on the spatial grid. Then the value of \mathbf{E} at the particle position \mathbf{x}_m is taken as the value at the center of the cell \mathcal{C}_j containing \mathbf{x}_m . At each time step, the approximated density, needed to solve the Poisson equation, is reconstructed over the spatial cells \mathcal{C}_j from the updated particle positions and velocities. To discretize (2.25), we use a semi-implicit first-order scheme [31]:

$$\begin{aligned} \mathbf{x}_m^{n+1} &= \mathbf{x}_m^n + h\mathbf{v}_m^{n+1}, \\ \mathbf{v}_m^{n+1} &= \mathbf{v}_m^* + h(\mathbf{v}_m^{n+1} \times \mathbf{B}_{ext}(t^n, \mathbf{x}_m^n) + \mathbf{E}(t^n, \mathbf{x}_m^n)), \end{aligned} \tag{2.26}$$

where $\mathbf{B}_{ext}(t^n, \mathbf{x}_m^n)$ denotes the external magnetic field computed at the particle location, which will be determined in the control problem discussed in the next Section 3. In the rest of the paper we will drop for simplicity the \perp in the notation and consequently we will write \mathbf{x} instead of \mathbf{x}_\perp and \mathbf{v} instead of \mathbf{v}_\perp .

3 Robust feedback control by an external magnetic field

We now describe the robust feedback control strategy for the uncertain Vlasov–Poisson–BGK system introduced in Section 2.1. We begin our analysis by computing the external magnetic field \mathbf{B}_{ext} which is, by hypothesis orthogonal to the plane identified by \mathbf{x} and consequently we set $\mathbf{B}_{ext} = (0, 0, B)$.

We discretize the time interval $[0, t_f]$ into subintervals of length h , and solving the following sequence of instantaneous optimal control problems:

$$\begin{aligned} \min_{B \in \mathcal{B}_{adm}} \mathcal{J}(B; f_N^0, f_N) &:= \int_t^{t+h} \mathcal{P} \left[\sum_{\ell \in \{\mathbf{x}, \mathbf{v}\}} \mathcal{D}(f_N, \psi_\ell)(\tau, \mathbf{z}) \right] d\tau + \\ &+ \frac{\gamma}{2} \int_t^{t+h} \mathcal{P} \left[\int_\Omega |B(\tau, \mathbf{x})|^2 f_N(\tau, \mathbf{x}, \mathbf{v}, \mathbf{z}) d\mathbf{x} d\mathbf{v} \right] d\tau, \end{aligned} \tag{3.1}$$

where \mathcal{P} is defined as in (2.13)–(2.14), and $B_{adm} = \{B|B \in [-M, M], M > 0\}$, with M denoting the maximum admissible magnetic field strength. The function $\mathcal{D}(f_N, \psi_\ell)(\tau, \mathbf{z})$ is defined in (2.11), and f_N denotes the empirical density.

Applying a semi-implicit rectangle rule to approximate the time integrals in (3.1), we obtain the discrete cost functional (3.1) as follows

$$\begin{aligned} \mathcal{J}^h(B; f_N^0, f_N) &= h\mathcal{P} \left[\sum_{\ell \in \{\mathbf{x}, \mathbf{v}\}} \mathcal{D}(f_N^{n+1}, \psi_\ell)(\tau, \mathbf{z}) \right] + \\ &+ \frac{h\gamma}{2} \mathcal{P} \left[\int_{\Omega} |B^{n+1}(\mathbf{x})|^2 f_N^{n+1}(\mathbf{x}, \mathbf{v}, \mathbf{z}) d\mathbf{x} d\mathbf{v} \right]. \end{aligned} \quad (3.2)$$

3.1 Derivation of an approximated feedback control

Our next step is to insert the explicit form of the empirical distribution (2.19) into (3.2), under the constraint imposed by the semi-implicit dynamics (2.22)–(2.26). However, the semi-implicit scheme gives rise to strong nonlinear couplings, which make the associated optimality system analytically intractable and prevent a closed-form computation of the control. To overcome this difficulty, we introduce a simplified explicit integrator. In contrast to the semi-implicit method, the explicit scheme allows us to compute the optimal magnetic field in closed form at each particle location. This field is then inserted into the semi-implicit scheme for the actual evolution of the dynamics. In this way, we preserve the accuracy and stability properties of the semi-implicit scheme, while using the explicit scheme only as a tool for control synthesis, since it is not suitable for the time evolution of the dynamics due to its well-known stability limitations.

From a practical view point, we replace the numerical scheme (2.22)–(2.26) with the explicit scheme:

$$\begin{aligned} x_m^{n+1}(\mathbf{z}) &= x_m^n(\mathbf{z}) + hv_{x_m}^{n+1}(\mathbf{z}), \\ y_m^{n+1}(\mathbf{z}) &= y_m^n(\mathbf{z}) + hv_{y_m}^{n+1}(\mathbf{z}), \\ v_{x_m}^{n+1}(\mathbf{z}) &= v_{x_m}^*(\mathbf{z}) + hv_{y_m}^*(\mathbf{z})B_m^{n+1} + hE_{x_m}^n(\mathbf{z}), \\ v_{y_m}^{n+1}(\mathbf{z}) &= v_{y_m}^*(\mathbf{z}) - hv_{x_m}^*(\mathbf{z})B_m^{n+1} + hE_{y_m}^n(\mathbf{z}), \\ v_{x_m}^*(\mathbf{z}) &= \theta_m^{\nu, h} v_{x_m}^n(\mathbf{z}) + (1 - \theta_m^{\nu, h})(U_{x_m}^n(\mathbf{z}) + \xi_m \sqrt{T_m^n(\mathbf{z})}), \\ v_{y_m}^*(\mathbf{z}) &= \theta_m^{\nu, h} v_{y_m}^n(\mathbf{z}) + (1 - \theta_m^{\nu, h})(U_{y_m}^n(\mathbf{z}) + \xi_m \sqrt{T_m^n(\mathbf{z})}), \end{aligned} \quad (3.3)$$

where B_m indicates the value of the parallel part of the magnetic field at the particle position (x_m, y_m) and with $\theta_m^{\nu, h} = \chi(\eta_m < e^{-\nu h})$ being the stochastic jump process parameter used for handling the collision part.

By direct computation assuming in (2.11) $\psi_x = y^{n+1}(\mathbf{z})$, $\psi_v = v_y^{n+1}(\mathbf{z})$, $\hat{\psi}_x = \hat{y}$, $\hat{\psi}_v = 0$, being \hat{y} a certain function of the particles state related to the fact that we want to avoid

the plasma to reach the boundaries by imposing a target average position and a target average velocity, we get

$$\begin{aligned} \mathcal{J}^{h,N}(B_m) = h\mathcal{P} \left[\sum_{m=1}^N \left(\frac{\alpha_x}{2} |y_m^{n+1}(\mathbf{z}) - \hat{y}|^2 + \frac{\beta_x}{2} |y_m^{n+1}(\mathbf{z}) - \bar{y}^n(\mathbf{z})|^2 + \right. \right. \\ \left. \left. + \frac{\alpha_v}{2} |v_{y_m}^{n+1}(\mathbf{z})|^2 + \frac{\beta_v}{2} |v_{y_m}^{n+1}(\mathbf{z}) - \bar{v}_y^*(\mathbf{z})|^2 \right) \right] + \frac{h\gamma}{2} \mathcal{P} \left[\sum_{m=1}^N |B_m|^2 \right], \end{aligned} \quad (3.4)$$

with $\alpha_x, \alpha_v, \beta_x, \beta_v, \gamma \geq 0$, and where

$$\bar{y}^n(\mathbf{z}) = \frac{1}{N} \sum_{m=1}^N y_m^n(\mathbf{z}), \quad \bar{v}_y^*(\mathbf{z}) = \frac{1}{N} \sum_{m=1}^N v_{y_m}^*(\mathbf{z}).$$

Now, the following Proposition holds true.

Proposition 1. *Assume the parameters to scale as*

$$\alpha_x \rightarrow \frac{\alpha_x}{h}, \quad \beta_x \rightarrow \frac{\beta_x}{h}, \quad \gamma \rightarrow \gamma h, \quad \nu \rightarrow \frac{\nu}{h}, \quad (3.5)$$

then the feedback control B_m associated to (3.4) reads as follows

$$B_m = \mathbb{P}_{[-M,M]} \left(\frac{\mathcal{P}[\mathcal{R}_x^{m,n}(\mathbf{z}) + \mathcal{R}_v^{m,n}(\mathbf{z})]}{\gamma + \mathcal{P}[\mathcal{S}_x^{m,n}(\mathbf{z}) + \mathcal{S}_v^{m,n}(\mathbf{z})]} \right), \quad (3.6)$$

where for any $m = 1, \dots, N$, $\gamma > 0$, we have

$$\begin{aligned} \mathcal{R}_x^{m,n}(\mathbf{z}) &= \alpha_x (y_m^n(\mathbf{z}) + h(v_{y_m}^{*,n}(\mathbf{z}) + hE_{y_m}^n(\mathbf{z}) - \hat{y})v_{x_m}^{*,n}(\mathbf{z}) + \\ &\quad + \beta_x (y_m^n(\mathbf{z}) + h(v_{y_m}^{*,n}(\mathbf{z}) + hE_{y_m}^n(\mathbf{z}) - \bar{y}^n(\mathbf{z}))v_{x_m}^{*,n}(\mathbf{z}), \\ \mathcal{R}_v^{m,n}(\mathbf{z}) &= \alpha_v (v_{y_m}^{*,n}(\mathbf{z}) + hE_{y_m}^n(\mathbf{z}))v_{x_m}^{*,n}(\mathbf{z}) + \\ &\quad + \beta_v (v_{y_m}^{*,n}(\mathbf{z}) + hE_{y_m}^n(\mathbf{z}) - \bar{v}_y^*(\mathbf{z}))v_{x_m}^*(\mathbf{z}), \\ \mathcal{S}_x^{m,n}(\mathbf{z}) &= (\alpha_x + \beta_x)(hv_{x_m}^{*,n}(\mathbf{z}))^2, \\ \mathcal{S}_v^{m,n}(\mathbf{z}) &= (\alpha_v + \beta_v)h(v_{x_m}^{*,n}(\mathbf{z}))^2, \end{aligned} \quad (3.7)$$

with $\alpha_x, \alpha_v, \beta_x, \beta_v \geq 0$, $\mathbb{P}_{[-M,M]}(\cdot)$ denoting the projection over the interval $[-M, M]$, $\mathcal{P}(\cdot)$ as in (2.13)-(2.14), and with

$$\begin{aligned} v_{x_m}^{*,n}(\mathbf{z}) &= \theta_m^\nu v_{x_m}^n(\mathbf{z}) + (1 - \theta_m^\nu)(U_{x_m}^n(\mathbf{z}) + \xi_m \sqrt{T_m^n(\mathbf{z})}), \\ v_{y_m}^{*,n}(\mathbf{z}) &= \theta_m^\nu v_{y_m}^n(\mathbf{z}) + (1 - \theta_m^\nu)(U_{y_m}^n(\mathbf{z}) + \xi_m \sqrt{T_m^n(\mathbf{z})}), \end{aligned} \quad (3.8)$$

being $\theta_m = \chi(\eta_m < e^{-\nu})$, with $\eta \sim \mathcal{U}([0, 1])$. In the limit $h \rightarrow 0$ the control at the continuous level reads,

$$B_m(t) = \mathbb{P}_{[-M,M]} \left(\frac{1}{\gamma} (\mathcal{P}[\mathcal{R}_x^m(t, \mathbf{z}) + \mathcal{R}_v^m(t, \mathbf{z})]) \right), \quad (3.9)$$

with

$$\begin{aligned}\mathcal{R}_x^m(t, \mathbf{z}) &= [\alpha_x(y_m(t, \mathbf{z}) - \hat{y}(t, \mathbf{z})) + \beta_x(y_m(t, \mathbf{z}) - \bar{y}(t, \mathbf{z}))]v_{x_m}^*(t, \mathbf{z}), \\ \mathcal{R}_v^m(t, \mathbf{z}) &= [\alpha_v v_{y_m}^*(t, \mathbf{z}) + \beta_v(v_{y_m}^*(t, \mathbf{z}) - \bar{v}_y^*(t, \mathbf{z}))]v_{x_m}^*(t, \mathbf{z}),\end{aligned}\tag{3.10}$$

being

$$\begin{aligned}v_{x_m}^*(t, \mathbf{z}) &= \theta_m^\nu v_{x_m}(t, \mathbf{z}) + (1 - \theta_m^\nu)(U_{x_m}(t, \mathbf{z}) + \xi_m \sqrt{T_m(t, \mathbf{z})}), \\ v_{y_m}^*(t, \mathbf{z}) &= \theta_m^\nu v_{y_m}(t, \mathbf{z}) + (1 - \theta_m^\nu)(U_{y_m}(t, \mathbf{z}) + \xi_m \sqrt{T_m(t, \mathbf{z})}),\end{aligned}$$

where $\theta_m = \chi(\eta_m < e^{-\nu})$, with $\eta \sim \mathcal{U}([0, 1])$.

Proof. We introduce the augmented Lagrangian

$$\mathcal{L}(B_m, \lambda_m) = \mathcal{J}^{h,N}(B_m) + \lambda_m(|B_m| - M),\tag{3.11}$$

with λ_m the Lagrangian multiplier. Then, for any $m = 1, \dots, N$, we solve the optimality system

$$\begin{cases} \partial_{B_m} \mathcal{L}(B, \lambda) = 0 \\ (\partial_{\lambda_m} \mathcal{L}(B, \lambda) = 0 \text{ and } \lambda_m \geq 0) \text{ or } (\partial_{\lambda_m} \mathcal{L}(B, \lambda) < 0 \text{ and } \lambda_m = 0). \end{cases}\tag{3.12}$$

We note that both the operators $\mathcal{P}[\cdot]$ in (2.13)-(2.14) satisfies

$$\partial_{B_m} \mathcal{P}[\psi(\cdot, \mathbf{z})] = \mathcal{P}[\partial_{B_m} \psi(\cdot, \mathbf{z})],$$

for any function $\psi(\cdot, \mathbf{z})$. Hence, from the first equation in (3.12) we get

$$\begin{aligned}\partial_{B_m} \mathcal{L} &= h\mathcal{P} [\alpha_x (y_m^n + h(v_{y_m}^* - hv_{x_m}^* B_m + hE_{y_m}^n) - \hat{y}) (-h^2 v_{x_m}^*) + \\ &\quad + \beta_x (y_m^n + h(v_{y_m}^* - hv_{x_m}^* B_m + hE_{y_m}^n) - \bar{y}^n) (-h^2 v_{x_m}^*) + \\ &\quad + \alpha_v (v_{y_m}^* - hv_{x_m}^* B_m + hE_{y_m}^n) (-hv_{x_m}^*) + \\ &\quad + \beta_v (v_{y_m}^* - hv_{x_m}^* B_m + hE_{y_m}^n - \bar{v}_y^*) (-hv_{x_m}^*)] + h\gamma B_m + \lambda_m \text{sign}(B_m) = 0,\end{aligned}$$

where we omit for simplicity the explicit dependence of the variables on \mathbf{z} , and where the operator $\mathcal{P}(\cdot)$ is defined as in (2.13)-(2.14). Then, if $\lambda_m \geq 0$, we get from the optimality condition (3.12) $|B_m| = M$. Consequently considering the two cases $B_m = M$ and $B_m = -M$ separately, under the scaling in (3.5), we get, setting $B_m = -M$

$$\begin{aligned}\frac{\lambda_m}{h^2} &= \mathcal{P} [\alpha_x (y_m^n + h(v_{y_m}^{*,n} + hv_{x_m}^{*,n} M + hE_{y_m}^n) - \hat{y}) (-v_{x_m}^{*,n}) + \\ &\quad + \beta_x (y_m^n + h(v_{y_m}^{*,n} + hv_{x_m}^{*,n} M + hE_{y_m}^n) - \bar{y}^n) (-v_{x_m}^{*,n}) + \\ &\quad + \alpha_v (v_{y_m}^{*,n} + hv_{x_m}^{*,n} M + hE_{y_m}^n) (-v_{x_m}^{*,n}) + \\ &\quad + \beta_v (v_{y_m}^{*,n} + hv_{x_m}^{*,n} M + hE_{y_m}^n - \bar{v}_y^{*,n}) (-v_{x_m}^{*,n})] - \gamma M \geq 0,\end{aligned}\tag{3.13}$$

with $v_{x_m}^{\star,n}, v_{y_m}^{\star,n}$ as in (3.8). From (3.13) we recover

$$\frac{\mathcal{P}[\mathcal{R}_x^{m,n}(\mathbf{z}) + \mathcal{R}_v^{m,n}(\mathbf{z})]}{\gamma + \mathcal{P}[\mathcal{S}_x^{m,n}(\mathbf{z}) + \mathcal{S}_v^{m,n}(\mathbf{z})]} \leq -M,$$

with $\mathcal{R}_\ell^{m,n}(\mathbf{z}), \mathcal{S}_\ell^{m,n}(\mathbf{z})$ for $\ell \in \{x, v\}$ as in (3.7). If conversely $\lambda_m \geq 0$ and $B_k = M$, by scaling the parameters as in (3.5), following a similar argument we have

$$\frac{\mathcal{P}[\mathcal{R}_x^{m,n}(\mathbf{z}) + \mathcal{R}_v^{m,n}(\mathbf{z})]}{\gamma + \mathcal{P}[\mathcal{S}_x^{m,n}(\mathbf{z}) + \mathcal{S}_v^{m,n}(\mathbf{z})]} \geq M. \quad (3.14)$$

If finally $\lambda_m = 0$, and by assuming the parameters to scale as in (3.5), from the first equation in (3.12) we have

$$B_m = \frac{\mathcal{P}[\mathcal{R}_x^{m,n}(\mathbf{z}) + \mathcal{R}_v^{m,n}(\mathbf{z})]}{\gamma + \mathcal{P}[\mathcal{S}_x^{m,n}(\mathbf{z}) + \mathcal{S}_v^{m,n}(\mathbf{z})]}, \quad (3.15)$$

and

$$-M \leq B_m \leq M. \quad (3.16)$$

All in all we get B_m defined as in (3.6). Finally, in the limit $h \rightarrow 0$ we recover equation (3.9). \square

3.2 Realization of the control via spatial interpolation

Proposition 1 provides a feedback control law based on the pointwise evaluation of the magnetic field at the position of each particle. However, such a requirement is not feasible from a technological perspective in realistic applications. To relax this constraint, we introduce an interpolation strategy by defining a set of fictitious spatial cells $C_k, k = 1, \dots, N_c$, partitioning the physical domain. Within this framework, the magnetic field acting on a particle located at position \mathbf{x}_m is approximated by the constant value of the field within the cell C_k that contains the particle. While this choice increases the complexity of the control problem, it leads to a more realistic and implementable setting. As mentioned in Section 2.1, we adopt the simplification that the magnetic field lines in the two dimensional setting considered can be approximated by horizontal lines, since the contribution of the poloidal component of the magnetic field is much more smaller than the toroidal one. Following the idea introduced in [40], we suppose the grid on which the magnetic field is reconstructed aligns with the magnetic field lines. Thus, for each $k = 1, \dots, N_c$, we define the piecewise constant control \hat{B}_k over the cell C_k by interpolating the pointwise control values B_m within the corresponding cell. For convenience, we denote by

$$\mathbf{B} = \mathcal{I}^\ell(\mathbf{B}_N, \mathbf{x}_c), \quad (3.17)$$

the vector $\mathbf{B} = [\hat{B}_1, \dots, \hat{B}_{N_c}]$ collecting the interpolated controls \hat{B}_k . Here, $\mathcal{I}^\ell(\cdot)$ denotes a piecewise-constant interpolation operator of order ℓ , \mathbf{x}_c is the vector of the positions

of the centers of the cells C_k , and $\mathbf{B}_N = [B_1, \dots, B_N]$ is the vector of pointwise controls B_m as defined in equation (3.9). We observe that the penalization term acting on the control is weighted by the distribution function f . Consequently, in regions where f is small, the corresponding magnetic field intensity B could, in principle, take large values without significantly affecting the overall cost. By introducing fictitious cells and enforcing a piecewise-constant control over each of them, the penalization acts uniformly at the cell level, ensuring a globally balanced regularization of the control. More generally, in the absence of spatial discretization, areas with low particle density contribute only marginally to the overall system dynamics. Hence, allowing locally larger control amplitudes in such regions would not substantially modify the global behavior of the solution. Algorithm 3.1 outlines the described procedure.

Algorithm 3.1 (PIC scheme and control in uncertain setting).

- Consider N_z collocation nodes z_j as outline in Algorithm 2.1.
- For each node z_j , sample the position and velocity of N particles (x_m^0, v_m^0) from the initial density, and compute the quantities in (3.7).
- Compute the value of B_m as in (3.9), choosing a suitable statistical operator to account for the uncertainty.
- Interpolate the values of the control B_m over the fictitious spatial cells C_k to obtain a piecewise constant control \hat{B}_k as in (3.17).
- for $n = 1$ to N_t
 1. for $j = 1$ to N_z
 - Associate to each particle in cell C_k the value of the control \hat{B}_k .
 - Update the particle position and velocities according to the semi-implicit PIC scheme (2.26), using the control previously computed.
 - Recompute the quantities in (3.7).
 - end for
 2. Compute the value of B_m as in (3.9), choosing a suitable statistical operator to account for the uncertainty.
 3. Interpolate the values of the control B_m over the fictitious spatial cells C_k to obtain a piecewise constant control \hat{B}_k as in (3.17).
 4. Reconstruct the quantities of interest as highlighted in Algorithm 2.1.
- end for

We emphasize that the control expression introduced in equation (3.17) is, in general, sub-optimal with respect to the reduced-horizon control problem (3.2)–(3.3) in the limit $h \rightarrow 0$, as it relies on an additional interpolation of the dynamics. Nevertheless, since the main objective is to confine the entire ensemble of particles within the physical domain and to assess the robustness of the control strategy, we employ the control defined in (3.17) within the semi-implicit dynamics (2.23)–(2.26), demonstrating its effectiveness in steering the plasma toward a desired configuration.

A comparison with an alternative control strategy, originally proposed in [2] and extended here to the uncertain setting, is provided in A. This highlights the improvements achieved by the feedback-based approach presented in this section.

Remark 1. We remark that the control B_m in equation (3.6) is of feedback type, since it depends on the particle positions and velocities at time t_n . From a numerical point of view, these quantities are readily available at each iteration of the scheme and are used to compute the control online, as outlined in Algorithm 3.1. Physically, this would correspond to accessing particle positions and velocities at each time step, which may not be directly feasible in practice. In general, however, the control could be reconstructed from sampled particle positions and velocities, so that knowledge of the full microscopic state of the system would not be required. To further bridge the gap between the idealized numerical setting and more realistic scenarios, we also include a test in which the control field is computed and then held fixed for a prescribed number of time steps before being updated again. This strategy mimics the effect of limited measurement or actuation frequency and demonstrates that the feedback approach remains effective under such practical constraints.

Remark 2. Note that by increasing the number of fictitious spatial cells C_k , it is possible to obtain a continuous representation of the control value, reconstructed on the physical spatial grid.

4 Numerical experiments

In this section, we present several numerical experiments aimed at demonstrating the effectiveness of the instantaneous control strategy, as described in the previous sections, in steering the plasma toward desired configurations. In particular, we focus on a variant of the classical Sod shock tube test and a modified version of the Kelvin–Helmholtz instability, both enhanced by the inclusion of collisions, electromagnetic effects, and uncertainty. We compare the system’s behavior with and without control to highlight the impact of the proposed strategy. Regarding uncertainty, we assume randomly distributed initial data following a uniform distribution over the interval $[0, 1]$, and we sample N_z Gaussian quadrature nodes accordingly.

4.1 2D Sod shock tube test

We focus on a two-dimensional Sod shock tube test, where we denote the position and velocity variables by $\mathbf{x} = (x, y)$ and $\mathbf{v} = (v_x, v_y)$, respectively. We consider the spatial domain $(x, y) \in [0, 1.5]^2$, imposing reflective boundary conditions in the y -direction and periodic boundary conditions in the x -direction. The initial distribution is given by

$$f_0(\mathbf{x}, \mathbf{v}, z) = \frac{\rho_0(\mathbf{x})}{2\pi T_0(\mathbf{x}, z)} \exp\left(-\frac{|\mathbf{v}|^2}{2T_0(\mathbf{x}, z)}\right), \quad (4.1)$$

with the initial density and temperature defined as

$$\rho_0(\mathbf{x}) = \begin{cases} 0.125, & \text{if } y \in [0, 0.5) \cup (1, 1.5], \\ 1, & \text{if } y \in [0.5, 1], \end{cases} \quad (4.2)$$

$$T_0(\mathbf{x}, z) = \begin{cases} 0.1 + 0.25z, & \text{if } y \in [0, 0.5) \cup (1, 1.5], \\ 1 + 0.25z, & \text{if } y \in [0.5, 1]. \end{cases}$$

The simulations are performed using $N = 10^7$ particles and a grid of $m_x \times m_y$ cells, with $m_x = m_y = 128$, for the reconstruction of macroscopic quantities. The final time is set to $t_f = 2$, with a time step $h = 0.05$. At each time step, for every node z_k , the empirical density (2.19) is reconstructed using a piecewise constant representation. The quantities of interests, such as the mean or the variance, are then computed following the procedure outlined in Algorithm 2.1.

4.1.1 Accuracy of the stochastic collocation method

First we validate the accuracy of the stochastic Gauss-Legendre formula when applied to the solution of the collisional Vlasov–Poisson equation with uncertainty, in particular in the context of a control strategy based on a worst-case scenario. We denote by $E_{N_z^{\text{ref}}}[\rho](T, \mathbf{x})$ the reference solution obtained with $N_z^{\text{ref}} = 256$ Gauss–Legendre nodes, and by $E_{N_z}[\rho](T, \mathbf{x})$ the corresponding approximation obtained with a lower number of nodes. The error at time $T = 0.2$, as a function of N_z , is defined as

$$\text{err}_{N_z}(T) = \left\| E_{N_z^{\text{ref}}}[\rho](T, \mathbf{x}) - E_{N_z}[\rho](T, \mathbf{x}) \right\|_{\infty}. \quad (4.3)$$

Figure 1 displays the error defined in (4.3) for two collisional regimes: $\nu = 0$ (left) and $\nu = 1000$ (right). We test the controlled case, where the magnetic field is defined as in (3.17), using the operator $\mathcal{P}(\cdot)$ defined either as in (2.14) (referred to as B_{max}) or as in (2.13) (referred to as B_{mean}). The results confirm that the method exhibits spectral accuracy with respect to the number of quadrature nodes N_z .

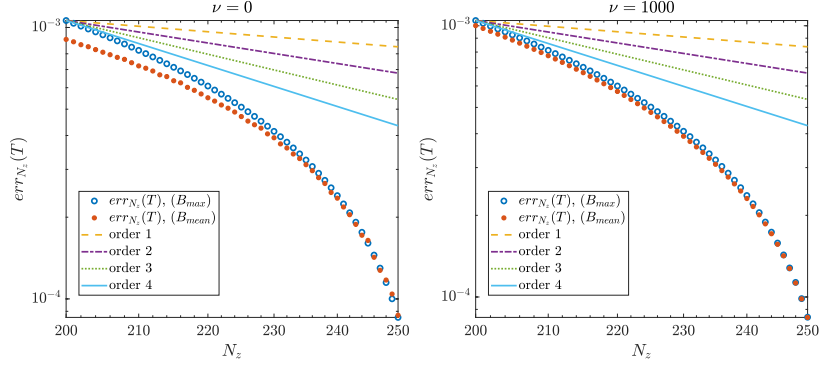


Figure 1: Two-dimensional Sod shock tube test with control. Norm of the error for $\nu = 0$ (on the left), $\nu = 1000$ (on the right).

4.1.2 Effectiveness of the control strategy

To assess the effectiveness of the control strategy, we compute the thermal energy at the boundaries for each value z_i , with $i = 1, \dots, N_z$, as

$$\mathcal{E}_b^n(z_i) = \frac{1}{2NN_b} \sum_{\mathcal{C}_j \in \Omega_b} \sum_{m=1}^N |\mathbf{v}_m^n(z_i) - U_b^n(z_i)|^2 \chi(\mathbf{x}_m^n \in \mathcal{C}_j), \quad (4.4)$$

where

$$\begin{aligned} U_b^n(z_i) &= \frac{1}{NN_b \rho_b^n(z_i)} \sum_{\mathcal{C}_j \in \Omega_b} \sum_{m=1}^N \mathbf{v}_m^n(z_i) \chi(\mathbf{x}_m^n \in \mathcal{C}_j), \\ \rho_b^n(z_i) &= \frac{1}{NN_b} \sum_{\mathcal{C}_j \in \Omega_b} \sum_{m=1}^N \chi(\mathbf{x}_m^n \in \mathcal{C}_j), \end{aligned} \quad (4.5)$$

and N_b denotes the number of cells $\mathcal{C}_j \in \Omega_b$, with $\Omega_b = [0, \Delta_y] \cup [1.5 - \Delta_y, 1.5]$. This choice corresponds to a region near the y -boundaries with width equal to one cell size $\Delta_y = 0.234$. In the uncontrolled case, enlarging the boundary region Ω_b is expected to increase the thermal energy at the boundaries, since particles entering this region contribute to local velocity fluctuations, thereby enhancing the effective kinetic energy and temperature. In contrast, under control we expect particles to remain confined near the center of the domain, which keeps the thermal energy at the boundaries low.

We begin by considering the uncontrolled case, setting $B(t, \mathbf{x}) = 1.5$. Figures 2–3–4 illustrate the system dynamics under three different collisional regimes: $\nu = 0$, $\nu = 10$, and $\nu = 1000$. In each figure, the first row displays snapshots of the mean density at times $t = 0.5$, $t = 0.75$, and $t = 1$. Superimposed in white are the mean trajectories of

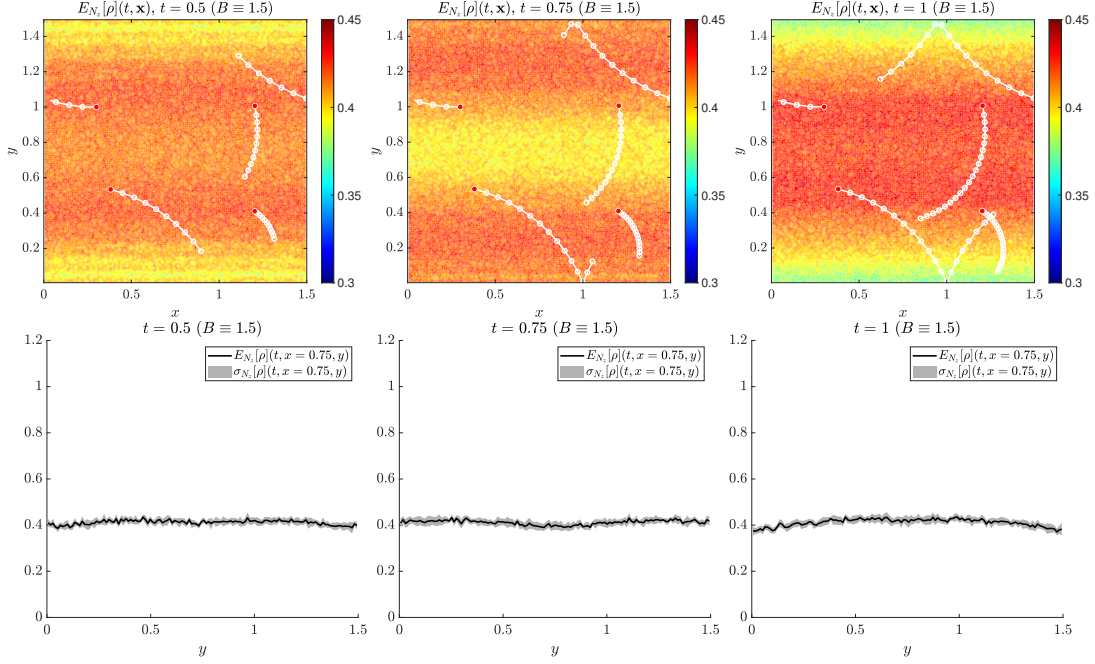


Figure 2: Two-dimensional Sod shock tube test with $B(t, \mathbf{x}) = 1.5$ and $\nu = 0$. Top row: snapshots of the mean density at different time instants. Bottom row: slices of the mean density at $x = 0.75$, with the corresponding standard deviation shown as a shaded area.

four randomly selected particles up to time t , with their initial mean positions highlighted in red. The second row shows slices of the mean density function at $x = 0.75$, taken at the same time instants, with the associated standard deviation represented as a shaded area. Initially, particles move toward the upper and lower boundaries of the domain, where they are reflected due to the imposed boundary conditions. As the collisional frequency ν increases, the diffusion of particles across the domain is progressively reduced. In the collisionless case ($\nu = 0$), particles exhibit strong diffusive behavior. In contrast, in the highly collisional regime ($\nu = 1000$), particles do not diffuse but instead oscillate around the center of the domain. The intermediate case ($\nu = 10$) corresponds to a quasi-collisional regime, where both diffusion and collisional effects are simultaneously present. Figure 5 shows the mean thermal energy at the boundaries along with its standard deviation for $\nu = 0$ (left), $\nu = 10$ (center), and $\nu = 1000$ (right). The thermal energy increases whenever particles collide with the boundaries. In the collisionless regime, the spatial diffusion of particles results in only minor variations in thermal energy. In contrast, in the quasi-collisional and fully collisional regimes, the thermal energy exhibits an oscillatory pattern, reflecting the behavior of the particle trajectories. We now consider the case in which the magnetic field is computed as the solution of a control problem aimed at minimizing the

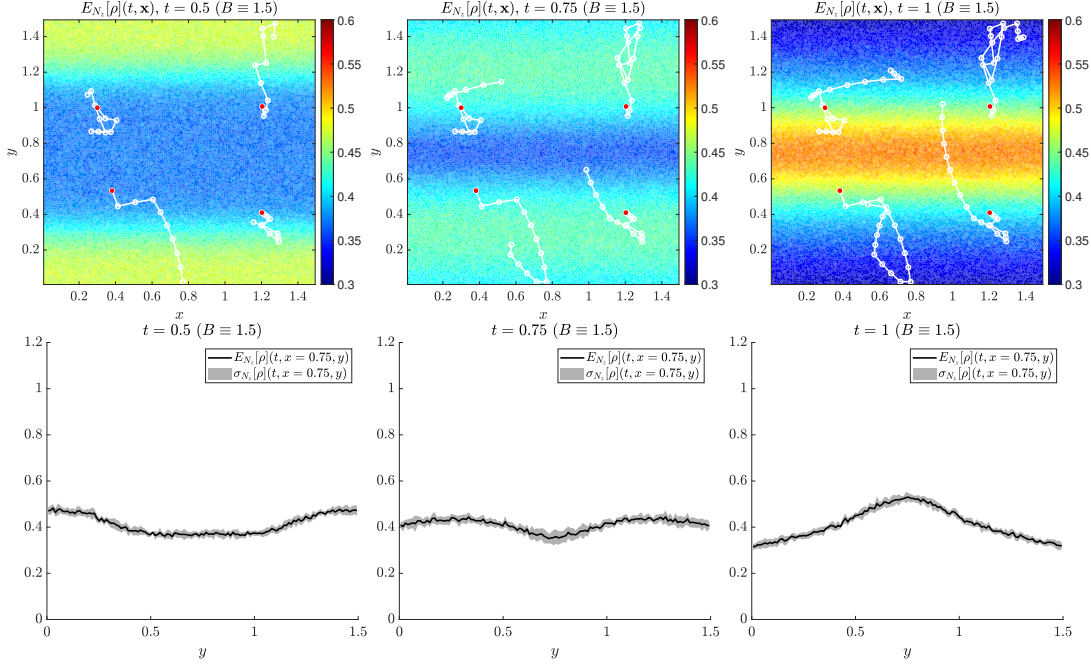


Figure 3: Two-dimensional Sod shock tube test with $B(t, \mathbf{x}) = 1.5$ and $\nu = 10$. Top row: snapshots of the mean density at different time instants. Bottom row: slices of the mean density at $x = 0.75$, with the corresponding standard deviation shown as a shaded area.

percentage of mass reaching the lower and upper boundaries of the domain. To this end, we assume that the spatial region where the control is active is divided into N_c horizontal cells, and we set $N_c = 4$, unless otherwise specified. We then perform a set of preliminary experiments to assess the sensitivity to the choice of the control parameters α_x , β_x , α_v , β_v , and γ . For simplicity, we assume to be in the fully collisional regime ($\nu = 1000$). Similar results can be obtained in the non-collisional regime and in the quasi-collisional one. Figure 6 shows the mean boundary thermal energy computed at time $t = 2$ as in (4.4). On the left, we test the correlation between $\alpha_x = \beta_x = 2, \dots, 10$ and $\alpha_v = \beta_v = 12, \dots, 20$, setting $\gamma = 2.5 \times 10^{-3}$ and $M = 50$. On the right, we fix $\alpha_x = 5$, $\beta_x = 2$, $\alpha_v = 15$, $\beta_v = 12$, $M = 50$, and we let γ to vary between 10^{-4} and 10^{-1} . Across all considered scenarios, the mean boundary thermal energy at the final time remains small and scales inversely with α_v , while showing no apparent dependence on α_x . Moreover, it decreases more rapidly and attains lower values as γ decreases. We then examined the correlation between the pairs (α_x, β_x) and (α_v, β_v) . The thermal energy at the boundaries remained essentially constant across all parameter combinations; accordingly, the corresponding plots are omitted for brevity. Other tests will be conducted later in this section to assess the effectiveness of the strategy as the maximum control strength and the initial temperature vary.

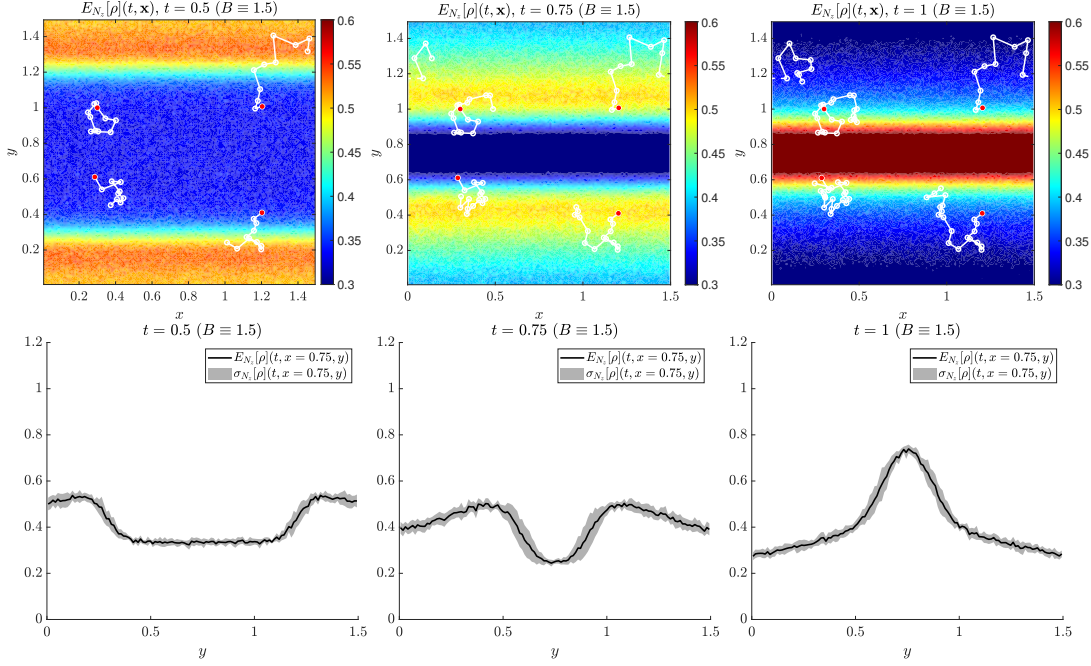


Figure 4: Two-dimensional Sod shock tube test with $B(t, \mathbf{x}) = 1.5$ and $\nu = 1000$. Top row: snapshots of the mean density at different time instants. Bottom row: slices of the mean density at $x = 0.75$, with the corresponding standard deviation shown as a shaded area.

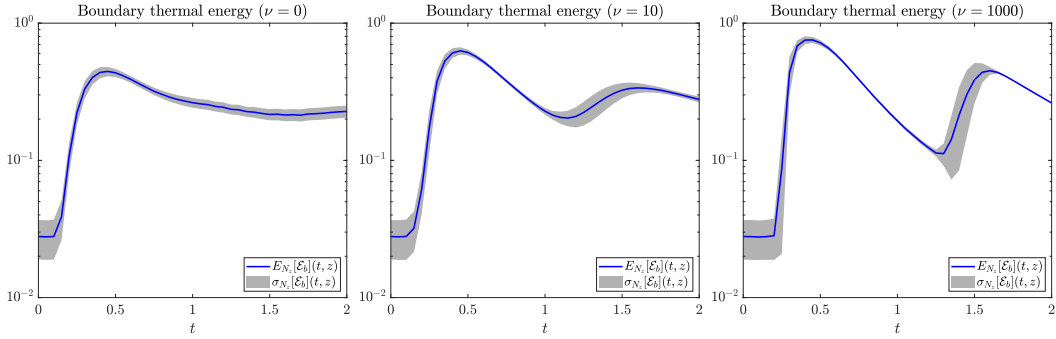


Figure 5: Two-dimensional sod shock tube test without control. Thermal energy at the boundaries for $\nu = 0$ (on the left), $\nu = 10$ (in the centre) and $\nu = 1000$ (on the right). The mean value is depicted in blue, while the standard deviation as a shaded area.

In the numerical experiments below, the parameters are specified as follows. The maximum control magnitude is fixed at $M = 50$, and the control parameters are chosen as

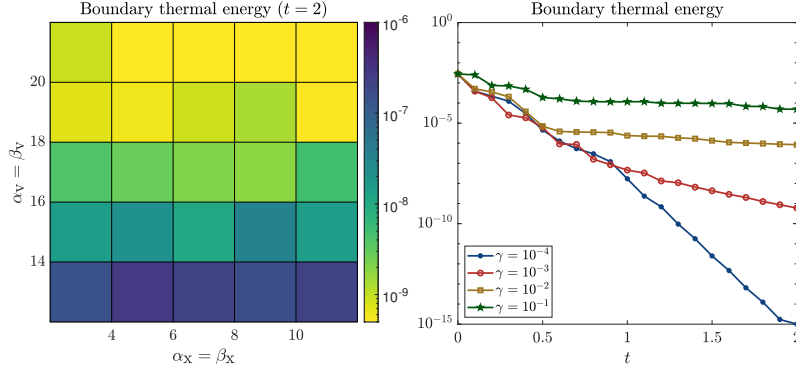


Figure 6: Two-dimensional Sod shock tube: preliminary test. On the left, mean boundary thermal energy at time $t = 2$ as $\alpha_x = \beta_x$ and $\alpha_v = \beta_v$ vary for $\gamma = 2.5 \times 10^{-3}$, and $M = 50$. On the right, mean boundary thermal energy for $\alpha_x = 5$, $\beta_x = 2$, $\alpha_v = 15$, $\beta_v = 12$, $M = 50$, as γ varies between 10^{-4} and 10^{-1} .

follows: $\alpha_x = 5$, $\beta_x = 2$, $\alpha_v = 15$, $\beta_v = 12$, and $\gamma = 2.5 \times 10^{-3}$. The target position is set to $\hat{y} = 0.75$, in order to drive the mass toward the center of the domain. Unless stated otherwise, the operator $\mathcal{P}(\cdot)$ is defined as in equation (2.14). The temperature at the boundaries is computed as

$$T_b^n(z_i) = \rho_b^n(z_i) \mathcal{E}_b^n(z_i),$$

for any $i = 1, \dots, N_z$, where $\rho_b^n(\cdot)$ and $\mathcal{E}_b^n(\cdot)$ are defined in equations (4.4)–(4.5). Figures 7–8–9 show the controlled dynamics for three different collisional regimes: $\nu = 0$, $\nu = 10$, and $\nu = 1000$. In each figure, the first row displays snapshots of the mean density at times $t = 0.5$, $t = 0.75$, and $t = 1$. The mean trajectories of four randomly selected particles are shown in white, with their initial positions highlighted in red. The second row shows slices of the mean density function at $x = 0.75$, corresponding to the same time instants, with the associated standard deviation represented as a shaded area. Additionally, the values of the magnetic field $B(t, \mathbf{x})$ in each cell C_k are displayed using a colorbar. Figure 10 shows, in the first row, the mean thermal energy at the boundaries, computed as in equation (4.4), for different values of ν , along with the corresponding standard deviation depicted as a shaded area. In all cases considered, the thermal energy decreases over time as a result of the confinement of particles near the center of the domain, highlighting the effectiveness of the adopted control strategy. In the second row, the temporal evolution of the magnetic field is shown for the same values of ν .

In Figure 11, we compare the thermal energy at the boundaries obtained using two different functionals within the control strategy. In particular, we consider the cases where $\mathcal{P}[\cdot]$ is defined as in equations (2.13) and (2.14), and denote the corresponding controls by B_{mean} and B_{max} , respectively. For both cases, we plot the mean thermal energy at the boundaries along with the corresponding standard deviation, represented as a shaded

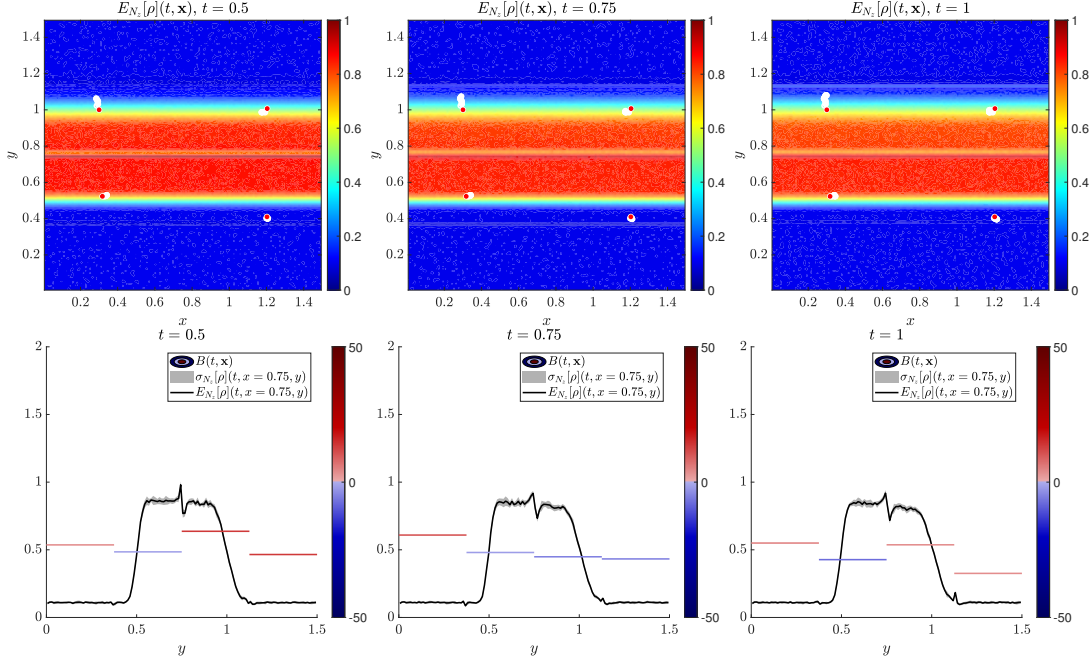


Figure 7: Two-dimensional Sod shock tube test with control and $\nu = 0$. Top row: snapshots of the mean density at different time instants. Bottom row: slices of the mean density at $x = 0.75$, with the corresponding standard deviation shown as a shaded area. The intensity of $B(t, \mathbf{x})$ in each cell C_k is represented by the colorbar.

area, under the same three collisional regimes previously considered. In all scenarios, the control strategy based on minimizing the worst-case behavior (B_{\max}) proves to be slightly more effective than the one based on the average behavior (B_{mean}) in achieving the desired confinement.

We now test the proposed strategy in long time by assuming $T = 6$, and that the magnetic field remains fixed for a certain number of time steps, n_{switch} . We rely on a simplify scenario, setting $z = 0$, and we suppose to be in the fully collisional regime, setting $\nu = 1000$. Figure 12 on the left shows the thermal energy at the boundary assuming $n_{\text{switch}} = 1, 2, 4, 6, 8, 10$, and in the center and on the right the value of the control in time for $n_{\text{switch}} = 2$ and $n_{\text{switch}} = 10$ respectively. While keeping the control fixed over multiple time steps proves effective in the short term, we observe that over longer times the thermal energy begins to oscillate. This indicates that, even though the values remain small, part of the mass gradually moves toward the y -boundaries of the domain, as expected. The shape of the control for $n_{\text{switch}} = 10$ suggests that in long time the strategy is no more effective, due to the presence of oscillations in the value of the thermal energy at the boundaries.

We conclude by testing the effectiveness of the proposed control strategy under more

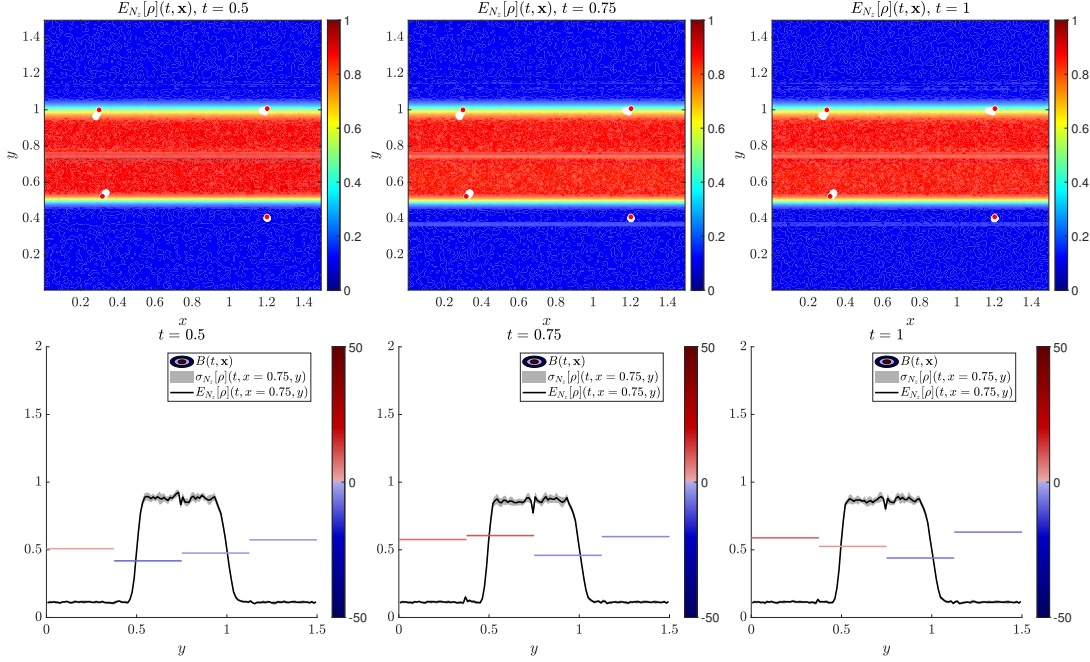


Figure 8: Two-dimensional Sod shock tube test with control and $\nu = 10$. Top row: snapshots of the mean density at different time instants. Bottom row: slices of the mean density at $x = 0.75$, with the corresponding standard deviation shown as a shaded area. The intensity of $B(t, \mathbf{x})$ in each cell C_k is represented by the colorbar.

challenging conditions, by increasing both the initial temperature of the plasma and the number of horizontal cells N_c over which the control is active. We consider a deterministic setting by fixing $z = 0$, and we assume the system operates in the fully collisional regime. Starting from the initial temperature T_0 defined in equation (4.2) (as used in the previous tests), we introduce three additional temperature profiles defined as follows:

$$\begin{aligned}
 \tilde{T}_0(\mathbf{x}) &= \chi(y \in [0, 0.5) \cup (1, 1.5]) + 10 \chi(y \in [0.5, 1]), \\
 \bar{T}_0(\mathbf{x}) &= 5 \chi(y \in [0, 0.5) \cup (1, 1.5]) + 50 \chi(y \in [0.5, 1]), \\
 \hat{T}_0(\mathbf{x}) &= 10 \chi(y \in [0, 0.5) \cup (1, 1.5]) + 100 \chi(y \in [0.5, 1]).
 \end{aligned} \tag{4.6}$$

The first row of Figure 13 shows, on the left, the evolution of thermal energy at the boundaries over time as the initial temperature increases, and on the right, the effect of varying the number of horizontal control cells N_c , for a fixed initial temperature $T_0(\mathbf{x}) = \hat{T}_0$. The second row reports the evolution in time of the control field for different values of N_c , again using \hat{T}_0 as the initial temperature. The results confirm that the effectiveness of the control strategy is inversely proportional to the initial plasma temperature, as expected. Moreover, the plot on the right suggests that increasing the number of horizontal cells does not lead

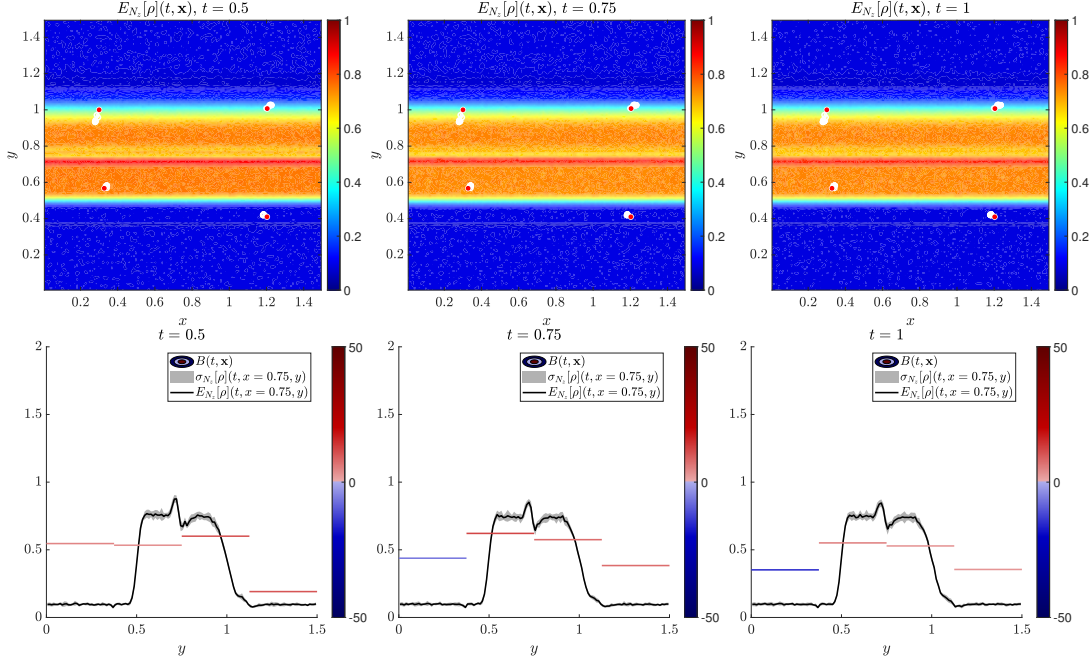


Figure 9: Two-dimensional Sod shock tube test with control and $\nu = 1000$. Top row: snapshots of the mean density at different time instants. Bottom row: slices of the mean density at $x = 0.75$, with the corresponding standard deviation shown as a shaded area. The intensity of $B(t, \mathbf{x})$ in each cell C_k is represented by the colorbar.

to significant improvements in thermal energy reduction.

Finally, we assess the effectiveness of the control in the case of larger plasma β larger. The plasma β

$$\beta \approx \frac{\rho T}{B^2}, \quad (4.7)$$

where ρ and T are the plasma density and temperature, and B is the magnetic field, is a dimensionless parameter that quantifies the ratio between the plasma thermal pressure and the magnetic pressure, measuring how effective the applied magnetic field is at confining the plasma [34]. A value of $\beta \ll 1$ indicates a magnetically dominated regime, where the plasma pressure is much smaller than the magnetic pressure and the magnetic field lines strongly determine the plasma dynamics. Conversely, $\beta \gg 1$ corresponds to a plasma-pressure dominated regime, where magnetic confinement becomes ineffective. For magnetically confined fusion plasmas, efficient operation requires intermediate values, where the plasma pressure is sufficiently high to sustain fusion reactions but still small enough to remain stably confined. In practice, stability constraints impose an upper bound on β , [53]. In particular, the

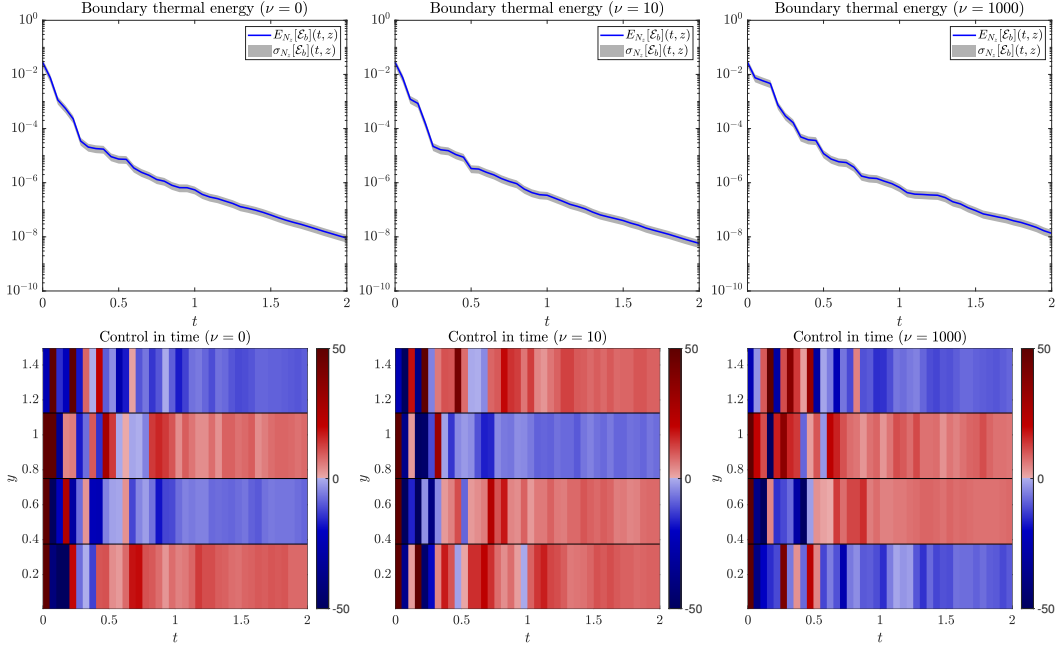


Figure 10: Two dimensional sod shock tube test with control. First row: mean thermal energy at the boundaries and the relative standard deviation depicted as a shaded area are shown. Second row: the value of the magnetic field is reported. On the left $\nu = 0$, in the centre $\nu = 10$, and on the right $\nu = 1000$.

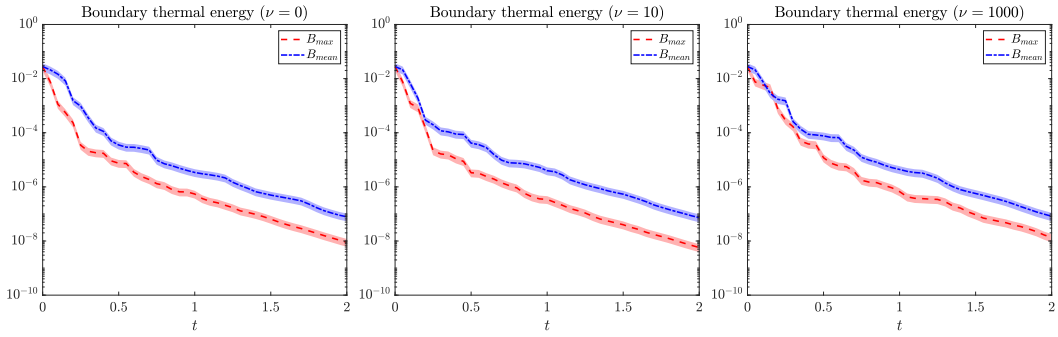


Figure 11: Two dimensional sod shock tube test with control. Mean thermal energy and relative standard deviation at the boundaries using $\mathcal{P}(\cdot)$ as defined in (2.14) (referred to as B_{max}) and (2.13) (referred to as B_{mean}). On the left $\nu = 0$, in the centre $\nu = 10$, and on the right $\nu = 1000$.

Troyon limit provides an empirical criterion for the maximum achievable β in a realistic Tokamak, that is $\beta \approx 0.01$ – 0.05 . Figure 14 (left) shows the boundary thermal energy at

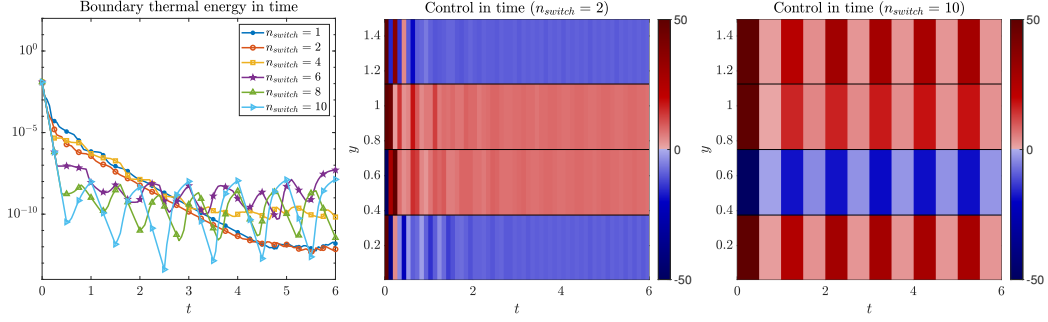


Figure 12: Two dimensional sod shock tube test with control. On the left, thermal energy at the boundaries as the magnetic field remains fixed for n_{switch} time steps. In the center and on the right, the value of the control B in time for $n_{switch} = 2$ and $n_{switch} = 10$.

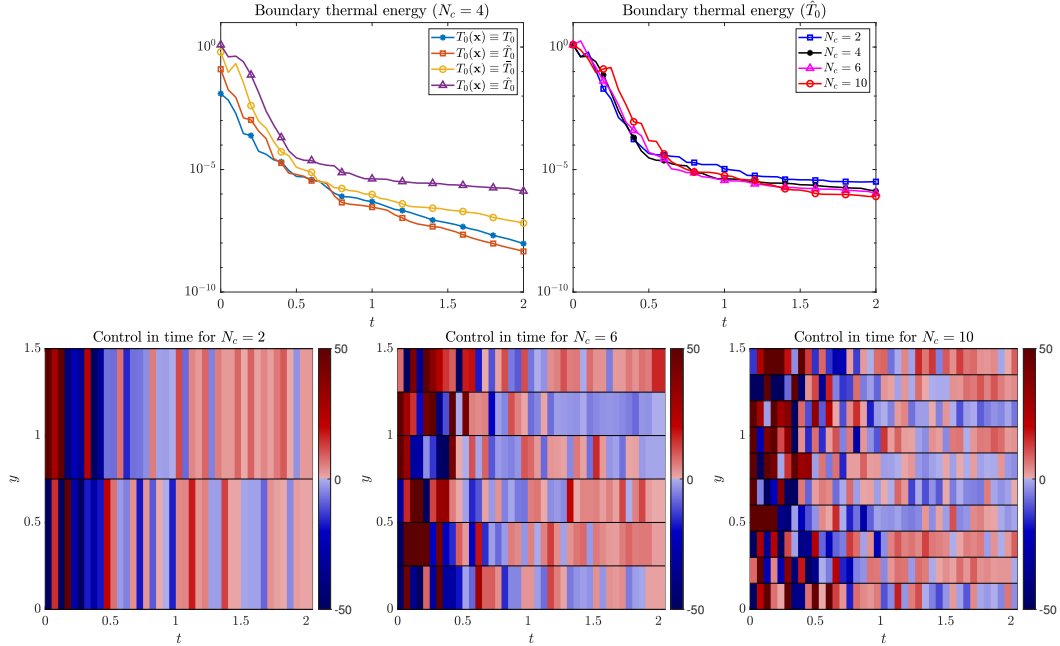


Figure 13: Two dimensional sod shock tube test with control. First row: thermal energy at the boundaries for different values of the initial temperature T_0 (left), thermal energy at the boundaries for different values of the number of cells N_c (right). Second row: the value of the control in time as N_c varies.

time $t = 2$, computed according to (4.4), for different values of the initial temperature and magnetic field strength M . The results indicate that the control strategy is effective except for cases with low M . On the right, Figure 14 shows the temporal evolution of the thermal

energy for different values of plasma β . The results indicate that in regimes with relatively large β , the control strategy becomes less effective, suggesting that further improvements may be necessary.

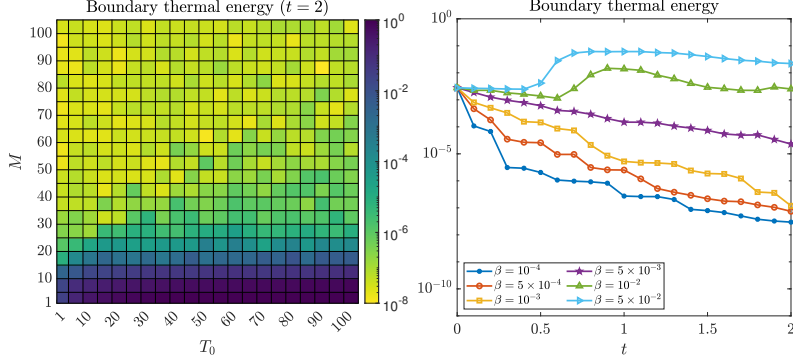


Figure 14: Two dimensional sod shock tube test with control. On the left, the boundary thermal energy at time $t = 2$ for different temperature values and control strengths. On the right, the boundary thermal energy in time as the plasma β varies.

4.2 Kelvin-Helmholtz instability

In this section, we examine a variant of the Kelvin-Helmholtz instability in the context of charged particles; see [19, 49, 9]. We conduct an analysis similar to that of the previous section, comparing the controlled and uncontrolled scenarios in the presence of both uncertainty and collisions. Periodic boundary conditions are imposed in the x -direction, and reflective boundary conditions are imposed in the y -direction. The computational domain is defined as $x \in [0, 40]$, $y \in [-5, 5]$, and the initial density is given by

$$\rho_0(\mathbf{x}) = \frac{1.5}{2\pi} \operatorname{sech}\left(\frac{y}{0.9}\right) (1 + \epsilon_0 \cos(3k_0x) + \epsilon_1 \sin(k_0x)), \quad (4.8)$$

with parameters $k_0 = 0.15$, $\epsilon_0 = 0.1$, and $\epsilon_1 = 0.001$. The initial distribution function is defined as

$$f_0(\mathbf{x}, \mathbf{v}, z) = f_0^+(\mathbf{x}, \mathbf{v}, z)\chi(y \geq 0) + f_0^-(\mathbf{x}, \mathbf{v}, z)\chi(y < 0), \quad (4.9)$$

where

$$f_0^\pm(\mathbf{x}, \mathbf{v}, z) = \frac{\rho_0(\mathbf{x})}{2\pi T_0(\mathbf{x}, z)} \exp\left(-\frac{(v_x \pm u_x)^2 + v_y^2}{2T_0(\mathbf{x}, z)}\right), \quad (4.10)$$

and $u_x = 1$ is the mean velocity in the x -direction. The initial temperature includes uncertainty and is defined by

$$T_0(\mathbf{x}, z) = 0.15 + 0.25z, \quad (4.11)$$

where $z \sim p(z)$ follows a uniform distribution over $[0, 1]$.

Figure 15 displays the estimated initial mean distribution and thermal energy, reconstructed over a grid of size $m_x \times m_y$, with $m_x = m_y = 128$. Simulations are performed using $N = 10^7$ particles, up to final time $T = 250$, with time step $h = 0.5$. In the uncontrolled case, we set $B = 1.5$, whereas in the controlled scenario, the control acts on $N_c = 4$ horizontal cells. The mean density and thermal energy at the boundaries are computed as in equation (4.4), with the boundary region defined as $\Omega_b = [-5, -4.8] \cup [4.8, 5]$.

4.2.1 Uncontrolled case

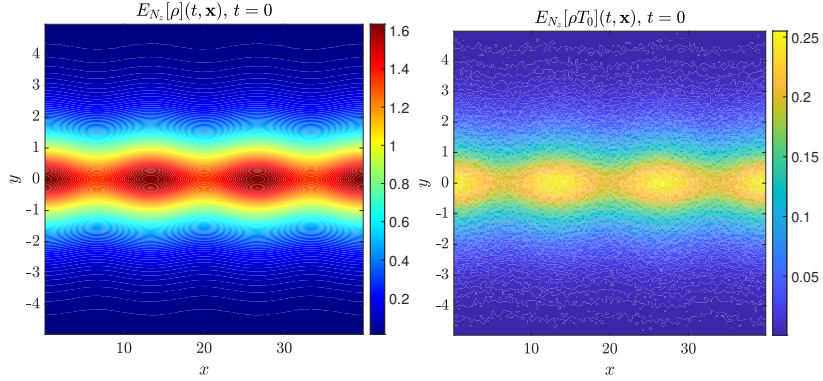


Figure 15: Kelvin-Helmholtz instability. Initial mean density and thermal energy.

Figure 16 shows the density field at times $t = 50$, $t = 75$, and $t = 200$ for the uncontrolled case with $B = 1.2$, across the three collisional regimes. In the fully collisional regime ($\nu = 1000$), the instability develops rapidly, whereas in the collisionless regime ($\nu = 0$) it emerges more gradually over time. An intermediate behavior is observed for the quasi-collisional case with $\nu = 10$. In Figure 17 the thermal energy at the boundary in time for $\nu = 0$ (on the left), $\nu = 10$ (in the centre), and $\nu = 1000$ (on the right) is shown. Once that the instability arises, the boundary thermal energy starts to increase.

4.2.2 Feedback controlled case

The case of the robust control is shown in Figure 18, for the non collisional regime. We set $\alpha_x = 5, \alpha_v = 15, \beta_x = 2, \beta_v = 12$, and $\gamma = 2.5 \times 10^{-3}$, $M = 100$, with target $\hat{y} = 0$, to confine the mass at the center of the domain as for the previous case. In the first row, three snapshots of the dynamics taken at time $t = 50$, $t = 75$ and $t = 200$ are depicted. In the second row the plot of the boundary thermal energy in time (on the left), and on control values in time in the four horizontal cells (on the right) can be observed. The figure demonstrates the effectiveness of the control strategy developed. Similar results are obtained in the quasi and fully collisional regimes for $\nu = 10$, and $\nu = 1000$, and

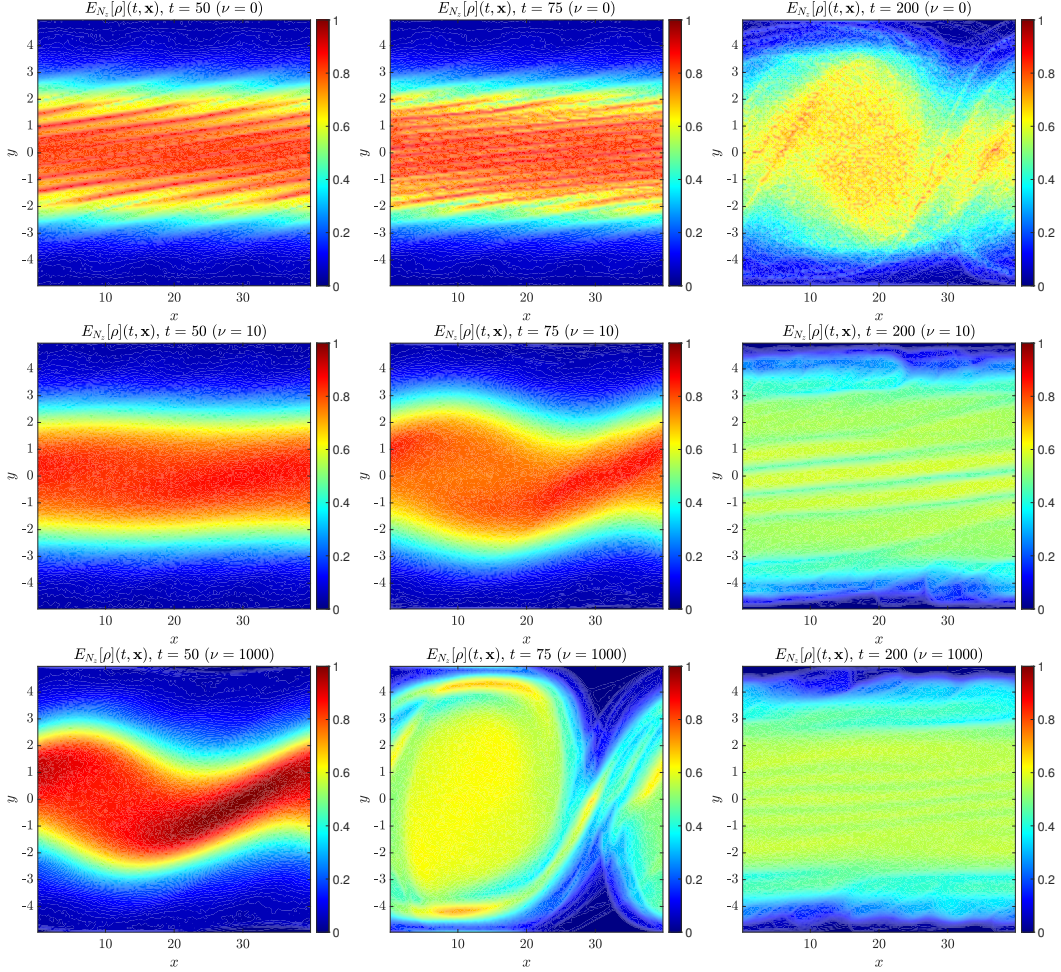


Figure 16: Kelvin-Helmholtz instability with $B(t, \mathbf{x}) = 1.2$. Mean density at $t = 50$, $t = 75$ and $t = 200$. First row: $\nu = 0$. Second row: $\nu = 10$. Third row: $\nu = 1000$.

are not shown for brevity. In this case, the control field is essentially time-independent, taking large values at the boundaries and weaker values at the center of the domain. This behavior closely resembles that of a magnetic mirror, although the configuration—with a strong magnetic field at the edges and a weaker one in the middle—is not prescribed a priori but rather obtained as the solution of the control problem [34]. When particles move from regions of low magnetic field to regions of high magnetic field, conservation of the magnetic moment implies that an increase in B produces a corresponding increase in v_y . Since the total kinetic energy must also be conserved, this increase in v_y is compensated by a decrease in v_x . Eventually, v_x vanishes and the particle reverses its motion, becoming confined along the magnetic field lines, which in our framework correspond to cell C_k .

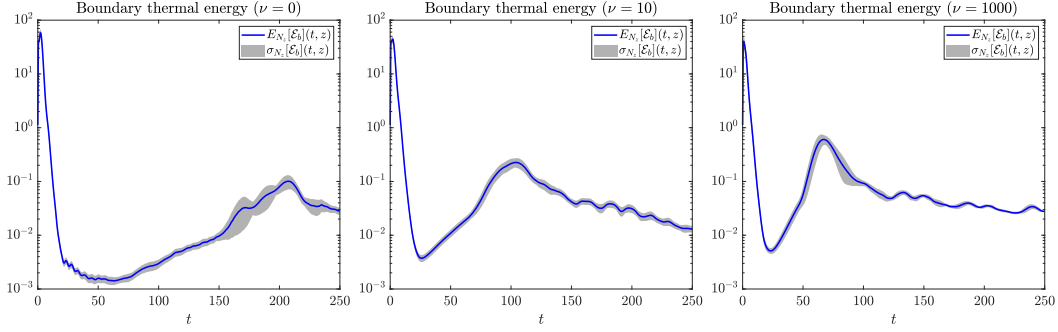


Figure 17: Kelvin-Helmholtz instability with $B(t, \mathbf{x}) = 1.2$. Thermal energy at the boundaries for $\nu = 0$ (on the left), $\nu = 10$ (in the centre) and $\nu = 1000$ (on the right). The mean value is depicted in blue, while the standard deviation as a shaded area.

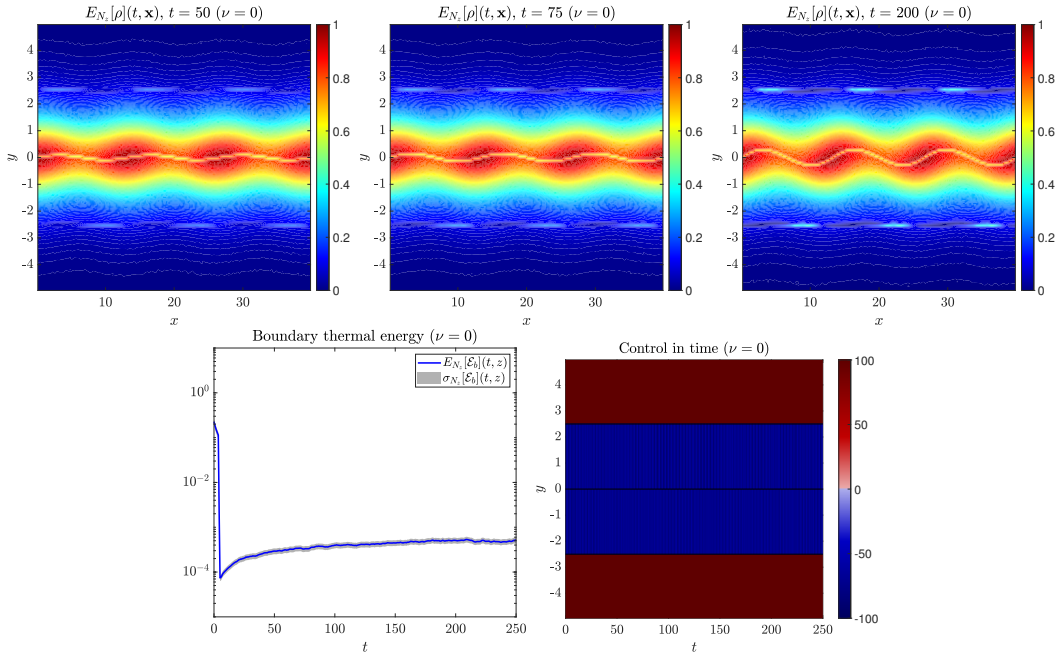


Figure 18: Kelvin-Helmholtz instability with control for $\nu = 0$. First row: mean density at $t = 50$, $t = 75$ and $t = 200$. Second row: thermal energy at the boundaries (on the left) and control (on the right). The mean thermal energy is depicted in blue, while the standard deviation as a shaded area.

Particles with larger initial v_y are reflected sooner, while those with smaller v_y may or may not be reflected depending on the field strength. In the Kelvin-Helmholtz instability, mass tends to accumulate near the boundaries of the internal fictitious cells, while some

particles are driven toward the outer boundary cells. This behavior arises from the initial particle distribution, which is characterized by small values of v_y . As a consequence, a slight increase in thermal energy appears at the boundaries, reaching values on the order of 10^{-4} .

In contrast, in the two-dimensional Sod test, particles start with a larger v_y component and are therefore reflected. In the short-time regime, the control exhibits oscillations aimed at steering the particles toward the desired configuration at the center of the domain. Over longer times, however, the control progressively reduces the v_y component of the particle velocities. As a result, the control field converges to a stationary profile, as illustrated in Figure 19, characterized by stronger intensity at the boundaries and weaker intensity at the center, thereby reproducing the magnetic mirror effect in this setting as well.

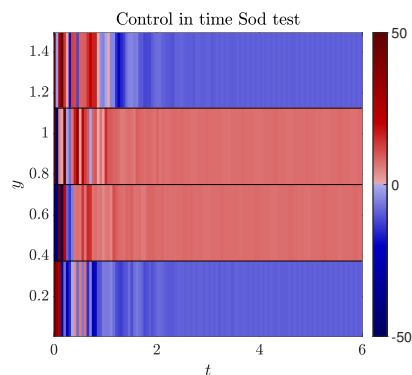


Figure 19: Two-dimensional Sod test: magnetic mirror effect. Value of the control in time.

5 Conclusions

In this work, we have proposed a new control strategy for the collisional Vlasov–Poisson–BGK system under uncertainty. The central idea is to develop an efficient instantaneous feedback control framework that steers the plasma toward a desired configuration through the application of an external magnetic field, which is constructed to be independent of the underlying randomness in the system.

To address the resulting optimization problem, we employed a semi-implicit Particle-In-Cell discretization for the Vlasov–Poisson system, combined with Monte Carlo sampling for the BGK collision process and a stochastic Gauss–Legendre quadrature method to represent uncertainty.

The control problem is formulated over a single time step, leading to an instantaneous feedback law derived via a simplified time integrator. The corresponding optimality system is solved through an augmented Lagrangian approach, ensuring enforcement of control constraints. The resulting feedback control is then integrated into the semi-implicit dynamics

by considering the continuous-time limit as the time step vanishes.

Numerical experiments validate the effectiveness of the proposed control strategy across various collisional regimes, demonstrating its ability to confine the plasma and prevent boundary interactions. As directions for future work, we plan to explore alternative uncertainty quantification strategies, including multi-fidelity control variates, which aim to reduce computational cost by coupling low- and high-fidelity models. We also intend to tackle the additional complexity arising from the full Maxwell–Vlasov–BGK system, and to investigate the incorporation of more realistic collision operators, such as the Landau operator, within the proposed control framework.

Acknowledgments

This work has been written within the activities of GNCS and GNFM groups of INdAM (Italian National Institute of High Mathematics). GA has been partially supported by MUR-PRIN Project 2022 No. 2022N9BM3N “Efficient numerical schemes and optimal control methods for time-dependent partial differential equations” financed by the European Union - Next Generation EU. GA and GD thank the European Union — NextGenerationEU, MUR–PRIN 2022 through the PNRR Project No. P2022JC95T “Data-driven discovery and control of multi-scale interacting artificial agent systems”. GD and FF thank the Italian Ministry of University and Research (MUR) through the PRIN 2020 project (No. 2020JLWP23) “Integrated Mathematical Approaches to Socio–Epidemiological Dynamics”. LP has been partially funded by the European Union– NextGenerationEU under the program “Future Artificial Intelligence– FAIR” (code PE0000013), MUR PNRR, Project “Advanced MATHematical methods for Artificial Intelligence– MATH4AI”. LP acknowledges the support by the Royal Society under the Wolfson Fellowship “Uncertainty quantification, data-driven simulations and learning of multiscale complex systems governed by PDEs” and by MIUR-PRIN 2022 Project (No. 2022KKJP4X), “Advanced numerical methods for time dependent parametric partial differential equations with applications”. The partial support by ICSC – Centro Nazionale di Ricerca in High Performance Computing, Big Data and Quantum Computing, funded by European Union – NextGenerationEU is also acknowledged.

A Comparison of different robust control strategies

In this Appendix, we first extend the control strategy introduced in [2] to the setting with uncertainty, and then compare it with the approach proposed in this work. Unlike the continuous control problem formulated in equation (2.9), where the control is computed for each particle and subsequently interpolated to obtain an average magnetic field, the strategy described in [2] directly computes a piecewise constant control (or magnetic field) within each fictitious cell C_k .

We briefly recall here the derivation of the instantaneous control strategy introduced in [2], extending it to account for uncertainty while, for simplicity, we assume a collisionless setting. We first formulate the problem at the continuous level and over a finite time horizon $[0, t_f]$ as follows

$$\min_{B \in \mathcal{B}_{adm}} \sum_{k=1}^{N_c} \mathcal{J}_k(B_k^{ext}; f_k, f_k^0), \quad \text{s.t. (2.2) - (2.4)}, \quad (\text{A.1})$$

where $f_k = f_k(t, \mathbf{x}, \mathbf{v}, \mathbf{z})$ corresponds to the normalized particle density restricted to a single cell C_k

$$f_k(t, \mathbf{x}, \mathbf{v}, \mathbf{z}) = \frac{f(t, \mathbf{x}, \mathbf{v}, \mathbf{z})}{\rho_k(t)}, \quad \rho_k(t) = \int_{\Omega_k} f(t, \mathbf{x}, \mathbf{v}, \mathbf{z}) d\mathbf{x}, d\mathbf{v},$$

with $\rho_k(t) > 0$ the total cell density and with $B = (B_1, \dots, B_{N_c})$ now representing the vector of z components of $\mathbf{B}(t, \mathbf{x})$ within each cell C_k , \mathcal{B}_{adm} the set of admissible controls such that $\mathcal{B}_{adm} = \{B_k^{ext} | B_k^{ext} \in [-M, M], M > 0, k = 1, \dots, N_c\}$, and where, for each $k = 1, \dots, N_c$, the cost functional is defined as follows

$$\begin{aligned} \mathcal{J}_k(B_k; f_k, f_k^0) = & \int_0^{t_f} (\mathcal{P}[\mathcal{D}(f_k)(t, \mathbf{z})] + \\ & + \frac{\gamma}{2} \mathcal{P} \left[\int_{\Omega_k} |B_k(t)|^2 f_k(t, \mathbf{x}, \mathbf{v}, \mathbf{z}) d\mathbf{x} d\mathbf{v} \right]) dt, \end{aligned} \quad (\text{A.2})$$

where $\gamma > 0$ is a penalization term, $\mathcal{P}[\cdot]$ is a suitable statistical operator taking into account the presence of the uncertainties, $\mathcal{D}(\cdot)$ aims at enforcing a specific configuration in the distribution function, and $\Omega_k = C_k \times \Omega_v$, being Ω_v the velocity domain. We consider a short time horizon of length $h > 0$ and formulate a time discretized optimal control problem through the functional \mathcal{J}_k restricted to the interval $[t, t+h]$, as follows

$$\min_{B_k \in \mathcal{B}_{adm}} \mathcal{J}_k^{N,h}(B_k; f_k^N, f_k^{N,0}), \quad (\text{A.3})$$

subject to a semi-implicit in time discretized Vlasov dynamics, fully explicit for the velocity terms

$$\begin{aligned} x_m^{n+1}(\mathbf{z}) &= x_m^n(\mathbf{z}) + hv_{x_m}^{n+1}(\mathbf{z}), \\ y_m^{n+1}(\mathbf{z}, \xi) &= y_m^n(\mathbf{z}) + hv_{y_m}^{n+1}(\mathbf{z}), \\ v_{x_m}^{n+1}(\mathbf{z}) &= v_{x_m}^n(\mathbf{z}) + hv_{y_m}^n(\mathbf{z})B_m^{n+1} + hE_{x_m}^n(\mathbf{z}), \\ v_{y_m}^{n+1}(\mathbf{z}) &= v_{y_m}^n(\mathbf{z}) - hv_{x_m}^n(\mathbf{z})B_m^{n+1} + hE_{y_m}^n(\mathbf{z}). \end{aligned} \quad (\text{A.4})$$

Using the rectangle rule for approximating the integral in time, and under the assumption that the magnetic field is independent of \mathbf{z} , the functional in (A.3) reads as follows

$$\mathcal{J}_k^{N,h}(B_k; f_k^N, f_k^{N,0}) = h \left(\mathcal{P}[\mathcal{D}(f_k^N)(t^{n+1}, \mathbf{z})] + \frac{\gamma}{2} |B_k|^2 \right). \quad (\text{A.5})$$

Here we assume

$$\mathcal{D}(f_k^N)(t, \mathbf{z}) = \sum_{\ell \in \{\mathbf{x}, \mathbf{v}\}} \mathcal{D}_k(f_k^N, \phi_\ell)(t^{n+1}, \mathbf{z}) \quad (\text{A.6})$$

with $\mathcal{D}_k(f_k^N, \phi_\ell)(\cdot, \mathbf{z})$ as in (2.11), where we replace the full domain Ω with Ω_k , for any $k = 1, \dots, N_c$. Thus, by setting $\phi_x = y^{n+1}$, $\phi_v = v_y^{n+1}$, $\hat{\phi}_{x,k} = \hat{y}_k$ and $\hat{\phi}_{v,k} = \hat{v}_{y_k}$, target states, and by direct computation over the empirical densities, we can rewrite the functional in (A.5) as

$$\begin{aligned} \mathcal{J}_k^{N,h}(B_k) = \mathcal{P} & \left[\frac{h\alpha_v}{2} |\bar{v}_{y,k}^{n+1}(\mathbf{z}) - \hat{v}_{y_k}|^2 + \frac{h\beta_v}{2N_k} \sum_{i \in C_k} |v_{y_i}^{n+1}(\mathbf{z}) - \bar{v}_{y,k}^n(\mathbf{z})|^2 + \right. \\ & \left. + \frac{h\alpha_x}{2} |\bar{y}_k^{n+1}(\mathbf{z}) - \hat{y}_k|^2 + \frac{h\beta_x}{2N_k} \sum_{i \in C_k} |y_i^{n+1}(\mathbf{z}) - \bar{y}_k^n(\mathbf{z})|^2 + \frac{h\gamma}{2} |B_k^{n+1}|^2 \right], \end{aligned} \quad (\text{A.7})$$

with

$$\bar{y}_k(\mathbf{z}) = \frac{1}{N_k} \sum_{j \in C_k} y_j(\mathbf{z}), \quad \bar{v}_{y,k}(\mathbf{z}) = \frac{1}{N_k} \sum_{j \in C_k} v_{y_j}(\mathbf{z}), \quad (\text{A.8})$$

denoting the mean position and velocity over cell C_k , $k = 1, \dots, N_c$. We extend now the result proved in [2] in the case of uncertainty.

Proposition 2. *Assume the parameters to scale as*

$$\alpha_x \rightarrow \frac{\alpha_x}{h}, \quad \beta_x \rightarrow \frac{\beta_x}{h}, \quad \gamma \rightarrow \gamma h, \quad (\text{A.9})$$

then the feedback control at cell C_k associated to (A.7) reads as follows

$$B_k = \mathbb{P}_{[-M,M]} \left(\frac{\mathcal{P}[\mathcal{R}_{v,k}^{N,n}(\mathbf{z}) + \mathcal{R}_{x,k}^{N,n}(\mathbf{z})]}{\gamma + \mathcal{P}[\mathcal{S}_{v,k}^{N,n}(\mathbf{z}) + \mathcal{S}_{x,k}^{N,n}(\mathbf{z})]} \right), \quad (\text{A.10})$$

where $\gamma > 0$,

$$\begin{aligned}
\mathcal{R}_{v,k}^{N,n}(\mathbf{z}) &= \alpha_v(\bar{v}_{y,k}^n(\mathbf{z}) + h\bar{E}_{y,k}^n(\mathbf{z}) - \hat{v}_{y_k})\bar{v}_{x,k}^n(\mathbf{z}) + \\
&\quad + \frac{\beta_v}{N_k} \sum_{i=1}^{N_k} [(v_{y_i}^n(\mathbf{z}) + hE_{y_i}^n(\mathbf{z}) - \bar{v}_{y,k}^n(\mathbf{z}))v_{x_i}^n(\mathbf{z})], \\
\mathcal{R}_{x,k}^{N,n}(\mathbf{z}) &= \alpha_x(\bar{y}_k^n(\mathbf{z}) + h(\bar{v}_{y,k}^n(\mathbf{z}) + h\bar{E}_{y,k}^n(\mathbf{z})) - \hat{y}_k)\bar{v}_{x,k}^n(\mathbf{z}) + \\
&\quad + \frac{\beta_x}{N_k} \sum_{i=1}^{N_k} [(y_i^n(\mathbf{z}) + h(v_{y_i}^n(\mathbf{z}) + hE_{y_i}^n(\mathbf{z})) - \bar{y}_k^n(\mathbf{z}))v_{x_i}^n(\mathbf{z})], \tag{A.11} \\
\mathcal{S}_{v,k}^{N,n}(\mathbf{z}) &= h \left(\alpha_v(\bar{v}_{x,k}^n(\mathbf{z}))^2 + \frac{\beta_v}{N_k} \sum_{i=1}^{N_k} (v_{x_i}^n(\mathbf{z}))^2 \right), \\
\mathcal{S}_{x,k}^{N,n}(\mathbf{z}) &= h^2 \left(\alpha_x(\bar{v}_{x,k}^n(\mathbf{z}))^2 + \frac{\beta_x}{N_k} \sum_{i=1}^{N_k} (v_{x_i}^n(\mathbf{z}))^2 \right),
\end{aligned}$$

and with $\mathbb{P}_{[-M,M]}(\cdot)$ denoting the projection over the interval $[-M, M]$. In the limit $h \rightarrow 0$ the control at the continuous level reads,

$$B_k(t) = \mathbb{P}_{[-M,M]} \left(\frac{1}{\gamma} (\mathcal{P} [\mathcal{R}_{v,k}^N(t, \mathbf{z}) + \mathcal{R}_{x,k}^N(t, \mathbf{z})]) \right), \tag{A.12}$$

with

$$\begin{aligned}
\mathcal{R}_{v,k}^n(t, \mathbf{z}) &= \alpha_v(\bar{v}_{y,k}(t, \mathbf{z}) - \hat{v}_{y_k})\bar{v}_{x,k}(t, \mathbf{z}) + \frac{\beta_v}{N_k} \sum_{i \in C_k} (v_{y_i}(t, \mathbf{z}) - \bar{v}_{y,k}(t, \mathbf{z}))v_{x_i}(t, \mathbf{z}), \\
\mathcal{R}_{x,k}^n(t, \mathbf{z}) &= \alpha_x(\bar{y}_k(t, \mathbf{z}) - \hat{y}_k)\bar{v}_{x,k}(t, \mathbf{z}) + \frac{\beta_x}{N_k} \sum_{i \in C_k} (y_i(t, \mathbf{z}) - \bar{y}_k(t, \mathbf{z}))v_{x_i}(t, \mathbf{z}).
\end{aligned}$$

We now focus on the two-dimensional Sod test discussed in Section 4.1, using the same numerical setting. We consider a collisionless regime and introduce uncertainty in the system by sampling $N_z = 10$ Gauss–Legendre nodes. We compare the instantaneous controls defined in equations (3.17) and (A.12), using the parameters $\alpha_x = 5$, $\beta_x = 2$, $\alpha_v = 15$, $\beta_v = 12$, $\gamma = 2.5 \times 10^{-3}$, and $M = 50$, with $\mathcal{P}(\cdot)$ defined as in equation (2.14). The simulation is carried out up to final time $t_f = 2$, with a time step $h = 0.05$. Figure 20 summarizes the results. On the left, we report the mean thermal energy at the boundaries along with the corresponding standard deviation. In the center and on the right, we show the magnetic field values. In the first row, the initial temperature is defined as in equation (4.2), while in the second row it corresponds to the high-temperature configuration given in equation (4.6) (last equation). In both cases, the new control strategy proposed in this work proves to be more effective in reducing thermal energy compared to the approach introduced in [2], with the improvement being particularly significant in high-temperature scenarios.

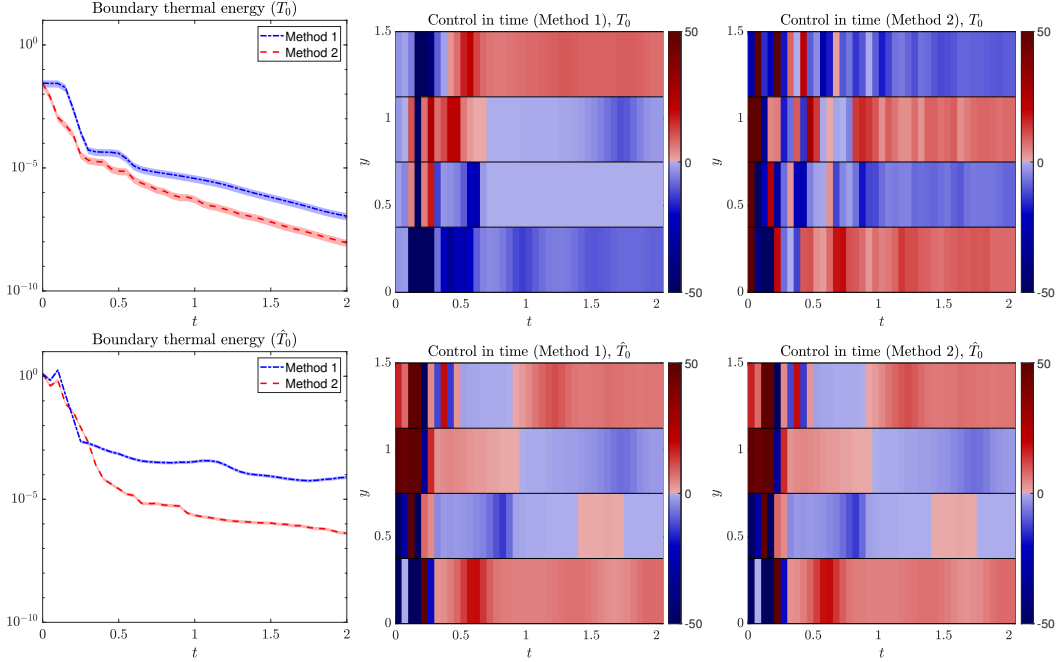


Figure 20: Two dimensional Sod shock tube test with control. Comparison between the two control strategies, (A.10) (Method 1) and (3.17) (Method 2) in terms of thermal energy at the boundaries (on the left) and of magnetic field value (in the center and on the right). The different lines depict the mean thermal energy at the boundaries, while the shaded areas represent the standard deviation.

References

- [1] G. Albi, Y.-P. Choi, M. Fornasier, and D. Kalise. Mean field control hierarchy. *Applied Mathematics & Optimization*, 76:93–135, 2017.
- [2] G. Albi, G. Dimarco, F. Ferrarese, and L. Pareschi. Instantaneous control strategies for magnetically confined fusion plasma. *Journal of Computational Physics*, page 113804, 2025.
- [3] J. Bartsch, P. Knopf, S. Scheurer, and J. Weber. Controlling a Vlasov–Poisson plasma by a Particle-In-Cell method based on a Monte Carlo framework. *SIAM Journal on Control and Optimization*, 62(4):1977–2011, 2024.
- [4] R. Belaouar, N. Crouseilles, P. Degond, and E. Sonnendrücker. An asymptotically stable semi-Lagrangian scheme in the quasi-neutral limit. *Journal of Scientific Computing*, 41:341–365, 2009.

- [5] J. Blum. *Numerical simulation and optimal control in plasma physics*. New York, NY; John Wiley and Sons Inc., 1989.
- [6] R. Caflisch, C. Wang, G. Dimarco, B. Cohen, and A. Dimits. A hybrid method for accelerated simulation of Coulomb collisions in a plasma. *SIAM Multiscale Modeling & Simulation*, 7(2):865–887, 2008.
- [7] R. E. Caflisch. Monte Carlo and Quasi Monte Carlo methods. *Acta Numerica*, 7:1–49, 1998.
- [8] S. Caprino, G. Cavallaro, and C. Marchioro. Time evolution of a Vlasov-Poisson plasma with magnetic confinement. *Kinetic & Related Models*, 5(4), 2012.
- [9] E. Chacon-Golcher, S. A. Hirstoaga, and M. Lutz. Optimization of Particle-In-Cell simulations for Vlasov–Poisson system with strong magnetic field. *ESAIM: Proc.*, 53:177–190, 2016.
- [10] G. Chen and L. Chacón. An implicit, conservative and asymptotic-preserving electrostatic Particle-In-Cell algorithm for arbitrarily magnetized plasmas in uniform magnetic fields. *Journal of Computational Physics*, 487:Paper No. 112160, 16, 2023.
- [11] C.-Z. Cheng and G. Knorr. The integration of the Vlasov equation in configuration space. *Journal of Computational Physics*, 22(3):330–351, 1976.
- [12] Y. Cheng, I. M. Gamba, F. Li, and P. J. Morrison. Discontinuous Galerkin methods for the Vlasov–Maxwell equations. *SIAM Journal on Numerical Analysis*, 52(2):1017–1049, 2014.
- [13] S. W. Chung, S. D. Bond, E. C. Cyr, and J. B. Freund. Regular sensitivity computation avoiding chaotic effects in Particle-In-Cell plasma methods. *Journal of Computational Physics*, 400:108969, 32, 2020.
- [14] J. Coughlin and J. Hu. Efficient dynamical low-rank approximation for the Vlasov-Ampère-Fokker-Planck system. *Journal of Computational Physics*, 470:Paper No. 111590, 20, 2022.
- [15] J. Coughlin and J. Hu. Efficient dynamical low-rank approximation for the Vlasov-Ampere-Fokker-Planck system. *Journal of Computational Physics*, 470:111590, 2022.
- [16] A. Crestetto, N. Crouseilles, and M. Lemou. Kinetic/fluid micro-macro numerical schemes for Vlasov-Poisson-BGK equation using particles. *Kinetic and Related Models*, 5(4):787–816, 2012.
- [17] N. Crouseilles, G. Dimarco, and M.-H. Vignal. Multiscale schemes for the BGK–Vlasov–Poisson system in the quasi-neutral and fluid limits. stability analysis and first order schemes. *SIAM Multiscale Modeling & Simulation*, 14(1):65–95, 2016.

- [18] N. Crouseilles and F. Filbet. Numerical approximation of collisional plasmas by high order methods. *Journal of Computational Physics*, 201(2):546–572, 2004.
- [19] N. Crouseilles, M. Mehrenberger, and E. Sonnendrücker. Conservative semi-Lagrangian schemes for Vlasov equations. *Journal of Computational Physics*, 229(6):1927–1953, 2010.
- [20] P. Degond. Asymptotic-preserving schemes for fluid models of plasmas. In *Numerical models for fusion*, volume 39/40 of *Panorama & Synthèses*, pages 1–90. Soc. Math. France, Paris, 2013.
- [21] P. Degond and F. Deluzet. Asymptotic-preserving methods and multiscale models for plasma physics. *Journal of Computational Physics*, 336:429–457, 2017.
- [22] P. Degond, F. Deluzet, L. Navoret, A.-B. Sun, and M.-H. Vignal. Asymptotic-preserving Particle-In-Cell method for the Vlasov-Poisson system near quasineutrality. *Journal of Computational Physics*, 229(16):5630–5652, 2010.
- [23] G. Dimarco, R. Caflisch, and L. Pareschi. Direct simulation Monte Carlo schemes for Coulomb interactions in plasmas. *Communications in Applied and Industrial Mathematics*, 1(1):72–91, 2010.
- [24] G. Dimarco, Q. Li, L. Pareschi, and B. Yan. Numerical methods for plasma physics in collisional regimes. *Journal of Plasma Physics*, 81(1), 2015.
- [25] G. Dimarco, L. Mieussens, and V. Rispoli. An asymptotic preserving automatic domain decomposition method for the Vlasov-Poisson-BGK system with applications to plasmas. *Journal of Computational Physics*, 274:122–139, 2014.
- [26] G. Dimarco and L. Pareschi. Multi-scale control variate methods for uncertainty quantification in kinetic equations. *Journal of Computational Physics*, 388:63–89, 2019.
- [27] G. Dimarco and L. Pareschi. Multiscale variance reduction methods based on multiple control variates for kinetic equations with uncertainties. *SIAM Multiscale Modeling & Simulation*, 18(1):351–382, 2020.
- [28] G. Dimarco, L. Pareschi, and M. Zanella. Micro-macro stochastic Galerkin methods for nonlinear Fokker-Planck equations with random inputs. *SIAM Multiscale Modeling & Simulation*, 22(1):527–560, 2024.
- [29] L. Einkemmer, Q. Li, C. Mouhot, and Y. Yue. Control of instability in a Vlasov-Poisson system through an external electric field. *Journal of Computational Physics*, 530:113904, 2025.

- [30] L. Einkemmer, Q. Li, L. Wang, and Y. Yunan. Suppressing instability in a Vlasov–Poisson system by an external electric field through constrained optimization. *Journal of Computational Physics*, 498:112662, 2024.
- [31] F. Filbet and L. M. Rodrigues. Asymptotically stable Particle-In-Cell methods for the Vlasov–Poisson system with a strong external magnetic field. *SIAM Journal on Numerical Analysis*, 54(2):1120–1146, 2016.
- [32] F. Filbet and L. M. Rodrigues. Asymptotically preserving Particle-In-Cell methods for inhomogeneous strongly magnetized plasmas. *SIAM Journal on Numerical Analysis*, 55(5):2416–2443, 2017.
- [33] F. Filbet and E. Sonnendrücker. Numerical methods for the Vlasov equation. In *Numerical Mathematics and Advanced Applications: Proceedings of ENUMATH 2001 the 4th European Conference on Numerical Mathematics and Advanced Applications Ischia, July 2001*, pages 459–468. Springer, 2003.
- [34] J. P. Freidberg. *Plasma physics and fusion energy*. Cambridge university press, 2008.
- [35] A. Gu, Y. He, and Y. Sun. Hamiltonian Particle-In-Cell methods for Vlasov–Poisson equations. *Journal of Computational Physics*, 467:111472, 2022.
- [36] J. Hu, S. Jin, and R. Shu. A stochastic Galerkin method for the Fokker–Planck–Landau equation with random uncertainties. *Theory, Numerics and Applications of Hyperbolic Problems II*, page 1, 2018.
- [37] S. Jin and Y. Zhu. Hypocoercivity and uniform regularity for the Vlasov–Poisson–Fokker–Planck system with uncertainty and multiple scales. *SIAM Journal on Mathematical Analysis*, 50(2):1790–1816, 2018.
- [38] P. Knopf and J. Weber. Optimal control of a Vlasov–Poisson plasma by fixed magnetic field coils. *Applied Mathematics & Optimization*, 81:961–988, 2020.
- [39] Y. Lin and S. Jin. Error estimates of a bi-fidelity method for a multi-phase Navier–Stokes–Vlasov–Fokker–Planck system with random inputs. *Kinetic and Related Models*, 17(5):807–837, 2024.
- [40] Z. Lu, G. Meng, E. Sonnendrücker, R. Hatzky, A. Mishchenko, F. Zonca, P. Lauber, and M. Hoelzl. Piecewise field-aligned finite element method for multi-mode nonlinear particle simulations in tokamak plasmas. *Journal of Plasma Physics*, 91(2):E48, 2025.
- [41] A. Medaglia, L. Pareschi, and M. Zanella. Stochastic Galerkin particle methods for kinetic equations of plasmas with uncertainties. *Journal of Computational Physics*, 479:112011, 2023.

- [42] A. Medaglia, L. Pareschi, and M. Zanella. Particle simulation methods for the Landau-Fokker-Planck equation with uncertain data. *Journal of Computational Physics*, 503:112845, 2024.
- [43] F. Nobile, R. Tempone, and C. G. Webster. A sparse grid stochastic collocation method for partial differential equations with random input data. *SIAM J. Num. Anal.*, 46(5):2309–2345, 2008.
- [44] L. Pareschi and G. Russo. An introduction to Monte Carlo methods for the Boltzmann equation. In *CEMRACS 1999 (Orsay)*, volume 10 of *ESAIM Proc.*, pages 35–76. Soc. Math. Appl. Indust., Paris, 1999.
- [45] L. Pareschi and G. Russo. Time relaxed Monte Carlo methods for the Boltzmann equation. *SIAM Journal on Scientific Computing*, 23(4):1253–1273, 2001.
- [46] L. Pareschi and S. Trazzi. Numerical solution of the Boltzmann equation by time relaxed Monte Carlo (TRMC) methods. *International journal for numerical methods in fluids*, 48(9):947–983, 2005.
- [47] G. Russo and F. Filbet. Semilagrangian schemes applied to moving boundary problems for the BGK model of rarefied gas dynamics. *Kinetic and related models*, 2(1):231–250, 2009.
- [48] L. Saint-Raymond. The gyrokinetic approximation for the Vlasov–Poisson system. *Mathematical Models and Methods in Applied Sciences*, 10(09):1305–1332, 2000.
- [49] E. Sonnendrücker, J. Roche, P. Bertrand, and A. Ghizzo. The semi-Lagrangian method for the numerical resolution of the Vlasov equation. *Journal of computational physics*, 149(2):201–220, 1999.
- [50] L. Spitzer, Jr. The stellarator concept. *Physics of Fluids*, 1:253–264, 1958.
- [51] W. T. Taitano, D. A. Knoll, and L. Chacón. Charge-and-energy conserving moment-based accelerator for a multi-species Vlasov-Fokker-Planck-Ampère system, part II: collisional aspects. *Journal of Computational Physics*, 284:737–757, 2015.
- [52] W. T. Taitano, D. A. Knoll, L. Chacón, and G. Chen. Development of a consistent and stable fully implicit moment method for Vlasov-Ampère particle in cell (PIC) system. *SIAM J. Sci. Comput.*, 35(5):S126–S149, 2013.
- [53] F. Troyon, R. Gruber, H. Saurenmann, S. Semenzato, and S. Succi. Mhd-limits to plasma confinement. *Plasma physics and controlled fusion*, 26(1A):209, 1984.
- [54] J. Wesson and D. J. Campbell. *Tokamaks*, volume 149. Oxford university press, 2011.

- [55] T. Xiao and M. Frank. A stochastic kinetic scheme for multi-scale plasma transport with uncertainty quantification. *Journal of Computational Physics*, 432:110–139, 2021.
- [56] D. Xiu and J. S. Hesthaven. High-order collocation methods for differential equations with random inputs. *SIAM Journal on Scientific Computing*, 27(3):1118–1139, 2005.
- [57] C. Yang and F. Filbet. Conservative and non-conservative methods based on hermite weighted essentially non-oscillatory reconstruction for Vlasov equations. *Journal of Computational Physics*, 279:18–36, 2014.
- [58] Y. Yudin, D. Coster, U. von Toussaint, and F. Jenko. Epistemic and aleatoric uncertainty quantification and surrogate modelling in high-performance multiscale plasma physics simulations. In *Computational Science – ICCS 2023*, volume 10476 of *Lecture Notes in Computer Science*, pages 572–586. Springer, 2023.
- [59] Y. Zhu and S. Jin. The Vlasov-Poisson-Fokker-Planck system with uncertainty and a one-dimensional asymptotic preserving method. *SIAM Multiscale Modeling & Simulation*, 15(4):1502–1529, 2017.